Intrinsic neuronal excitability and spontaneous activity underlie cortical abnormalities upon Nr2f1/COUP-TFI deficiency

Isabel del Pino[1°], Chiara Tocco[2*], Elia Magrinelli[2*#], Andrea Marcantoni[3*], Celeste Ferraguto[2], Giulia Tomagra[3], Christian Alfano[2+], Xavier Leinekugel[1&], Andreas Frick[1&] and Michèle Studer[2&@]*

[1]Université de Bordeaux, Inserm, Neurocentre Magendie, Bordeaux, France.

[2]Université Côte d'Azur, CNRS, Inserm, iBV, France

[3]Università di Torino, Dipartimento di Scienza e Tecnologia del Farmaco, Torino, Italy

*co-first authors

&co-last senior authors

°Present address: Centro de Investigación Príncipe Felipe, Valencia, Spain

#Present address: Département des Neurosciences Fondamentales, Université de Lausanne, Switzerland

+Present address: GIGA Stem Cells, University of Liège, Liège, Belgium

@Corresponding author:

Michèle Studer

iBV - Institut de Biologie Valrose

Univ. Nice Sophia Antipolis

Centre de Biochimie ; UFR Sciences

Parc Valrose, 28 avenue Valrose

06108 Nice Cedex 2

France

Tel.: +33 489150720

e-mail: Michele.studer@unice.fr

ABSTRACT

The formation of functionally different areas in the cerebral cortex results from a timely regulated interaction between intrinsic genetic mechanisms and electrical activity. However, whether and how transcriptional regulation influences spontaneous activity intrinsic to the neocortex during critical periods of corticogenesis is poorly elucidated. Here, we used mice deficient for cortical *Nr2f1* (also known as *COUP-TFI*) to investigate how a genetic-determinant of somatosensory area-identity influences immature neural excitability and network activity generated within the neocortex. We found that loss of *Nr2f1* alters intrinsic excitability and morphological features of pyramidal neurons during early postnatal stages. We also identified voltage-gated ion channels regulated by *Nr2f1* during a critical time window of somatosensory area specification. Accordingly, *Nr2f1* loss impacted on spontaneous network activity and synchronization at perinatal stages. Together, our data suggest that genetic specification of cortical area identity relies on intrinsic bioelectrical properties regulating patterns of spontaneous activity intrinsic to the neocortex.

INTRODUCTION

The area- and cell-type specific organization of the mammalian neocortex is a process involving coordinated interactions between cell intrinsic genetic programs and neural activity, an essential feature in specifying the composition and organization of neural circuits during all stages of development (Jabaudon, 2017, Simi and Studer, 2018). Before experience shapes neuronal circuits via sensory-driven activity, the developing cortex is genetically primed to establish patterns of spontaneous activity, which autonomously synchronize large groups of neurons independently of sensory stimulation (Andreae and Burrone, 2018, Kirischuk et al., 2017, Anton-Bolanos et al., 2019). These early patterns of spontaneous activity are thought to set the initial blueprint of cortical network organization. Hence, altering spontaneous activity during development can disrupt formation of functional neural circuits (Kirkby et al., 2013, Li et al., 2013).

In the neocortex, patterns of local spontaneous activity are already present during prenatal and early postnatal stages and contribute to the development of neuronal circuits (Luhmann and Khazipov, 2018). Although cortical areas comprise a variety of circuits, there are nevertheless striking similarities in some aspects of the mechanisms used to generate spontaneous activity. Calcium (Ca^{2+}) transients have been reported already at embryonic day E16, most probably generated in proliferating radial glia cells, as spatially restricted and slowly propagating calcium waves (Kirischuk et al., 2017). Immature neurons express voltage-dependent ion channels, responsible for a highly synchronized spontaneous activity within small neuronal networks (Luhmann et al., 2016). Certain features of immature cells, including high membrane resistance and prominent low-threshold calcium currents, seem to enhance excitability in neurons receiving little afferent sensory input (Moody and Bosma, 2005).

Besides spontaneous activity, the neocortical primordium is also under the control of distinct morphogens that establish proper coordinates along the developing anteroposterior and dorsoventral cortical axes (Greig et al., 2013, O'Leary and Sahara, 2008, Alfano and Studer, 2012). Functioning in a dose-, context- and time-dependent manner, these signaling pathways modulate gradient expression of area patterning genes, such as *Pax6*, *Sp8*, *Emx2* and *Nr2f1* (also known as COUP-TFI), among others. These transcription factors will cooperatively regulate

cell identity specification in cortical progenitors and early postmitotic neurons building a rough primordial areal map, known as protomap, which will be refined by sensory-evoked activity during postnatal stages (Simi and Studer, 2018). Alterations in genetic dosage of these factors alter the size and position of primordial area maps with severe consequences in cell-type specification and circuit formation (Greig et al., 2013, Jabaudon, 2017). Although the interaction between patterning genes and onset of spontaneous activity during primary area specification has been hypothesized, there is still no clear evidence on how this interaction is perpetrated.

To tackle this question, we used mice deficient for the nuclear receptor *Nr2f1*, a key transcriptional regulator during cortical development (Armentano et al., 2007), as a genetic model of area and laminar misspecification. As a member of the superfamily of steroid hormone receptors, *Nr2f1* represents a well-studied area patterning gene, which impinges sensory identity predominantly in early postmitotic cells during neocortical area mapping, and controls neuronal migration and differentiation (Alfano et al., 2014, Tomassy et al., 2010, Alfano et al., 2011, Faedo et al., 2008). Haploinsufficiency of the human *NR2F1* gene leads to an emerging genetic neurodevelopmental disorder called Bosch-Boonstra-Schaaf Optic Atrophy Syndrome (BBSOAS) (Bertacchi et al., 2019). Patients affected by this autosomal-dominant disorder exhibit several clinical features, such as intellectual disability, epileptic seizures, autistic-like traits, affected fine motor coordination and optic atrophy, among others (Bosch et al., 2014, Chen et al., 2016). In mice, *Nr2f1* deficiency in the cortex results in impaired primary somatosensory (S1) specification, delayed radial migration and abnormal laminar specification, particularly layer V pyramidal neurons, leading to distinct motor and cognitive impairments (Alfano et al., 2014, Armentano et al., 2007, Tomassy et al., 2010, Contesse et al., 2019). We employed this mouse model presenting severe area- and cell-type specific defects within the S1 to investigate whether and how spontaneous activity intrinsic to the cortex is altered during early stages of neocortical area and laminar specification. Our data show that glutamatergic pyramidal neurons, and particularly layer V neurons, undergo changes of intrinsic membrane excitability along with neuroanatomical and structural alterations within the immature cortex. Furthermore, we disclosed that altered levels of voltage-gated ion channels, and particularly HCN1, transcriptionally controlled by Nr2f1, underlie an aberrant state

of neural excitability in the early postnatal neocortex. Finally, we found that alterations observed at the electrophysiological, molecular and morphological levels correlate with altered Ca^{2+} bursts, network firing activity and synchronization events of *Nr2f1* mutant cortices at perinatal stages, before sensory evoked activity has taken place. Together, our data suggest that Nr2f1 controls cortical area patterning through the modulation of spontaneous activity intrinsic to the neocortex. This newly described function is accomplished by the transcriptional modulation of a plethora of channels involved in modulating intrinsic excitability as well as morphological and structural features of layer V pyramidal neurons.

RESULTS

Abnormal intrinsic electrophysiological properties in early postnatal *Nr2f1*-deficient cortical layer V pyramidal neurons

To address whether neural activity intrinsically generated within the neocortex could be regulated by area patterning genes such as *Nr2f1*, we employed a mutant mouse in which *Nr2f1* is exclusively deleted from the cortex without affecting thalamic differentiation (named thereof *Nr2f1cKO*) (Armentano et al., 2007). As intrinsic electrophysiological properties are major determinants of spontaneous neural activity, we first examined the state of intrinsic excitability of layer V glutamatergic pyramidal neurons (LVPNs), described to be abnormally specified in *Nr2f1cKO* mouse somatosensory cortices (Tomassy et al., 2010, Harb et al., 2016), through whole-cell recordings. We employed acute brain slices from *Ctrl* and *Nr2f1cKO* mouse pups during postnatal day (P)5–P8, as critical time points of early cortical circuit establishment. To assess for changes in intrinsic electrophysiological properties in a cell type-specific manner, we selected those neurons that were identified as LVPNs through *post-hoc* biocytin-filling, immunohistochemistry and morphological reconstruction. From 57 neurons recorded, we could identify 19 *Ctrl* and 28 *Nr2f1cKO* as neurons allocated in the layer V (**Figure 1**). All LVPNs from *Ctrl* and mutant brains displayed a slow-adapting regular spiking firing pattern (**Figure 1A**). Multivariate statistical analysis of intrinsic electrophysiological parameters revealed that *Nr2f1cKO* LVPNs clearly segregate from the *Ctrl* population (**Figure 1B)**. Notably, specific changes in passive and active electrophysiological properties

149 were observed in *Nr2f1cKO* neurons. Mutant LVPNs displayed a significantly more
150 depolarized resting membrane potential, a decreased rheobase and diminished
151 action potential amplitude when compared to *Ctrl* LVPNs. Interestingly, *Nr2f1cKO*
152 LVPNs also exhibited a significantly reduced voltage sag in response to
153 hyperpolarizing current steps, suggesting reduced I_h currents compared to *Ctrl*
154 LVPNs (**Figure 1C)**. No significant changes in input resistance, action potential
155 threshold, action potential half-width, inter-spike interval, membrane time constant
156 or input/output function were observed in mutant LVPNs (**Figure 1 – figure**
157 **supplement 1, table supplement 1**). Taken together, this first functional
158 characterization suggests that Nr2f1 deficiency specific to the developing cortex
159 leads to alterations in intrinsic excitability of immature LVPNs in the prospective
160 somatosensory region.
161
162 **Reduced dendritic complexity of LVPNs in *Nr2f1* mutant cortices**
163 To assess whether abnormal intrinsic excitability of mutant LVPNs was accompanied
164 by changes in somatodendritic morphology, we reconstructed and analyzed the
165 morphology of biocytin-labelled *Ctrl* and *Nr2f1cKO* P7 LVPNs (**Figure 2A,B**). We first
166 evaluated dendritic arbor geometry and complexity by performing Sholl analysis
167 (**Figure 2C – figure supplement 1A**). Comparison of Sholl profiles showed that
168 *Nr2f1cKO* LVPNs have a significantly reduced proximal dendritic branching (20-
169 100 m from the soma) when compared to *Ctrl* LVPNs, whereas minor or no
170 differences were observed in distal regions (**Figure 2 – figure supplement 1A**).
171 Next, to evaluate more specific features of dendrite geometry, we assessed the basal
172 dendrite complexity index (DCI), arbor length, number of primary dendrites,
173 branching points and tips, and oblique formations of basal and apical dendrites
174 (**Figure 2D-H; Figure 2 -figure supplement 1B-D**). Although no significant changes
175 were observed in apical and lateral dendrite geometry between *Ctrls* and *Nr2f1cKOs*
176 (**Figure 2 – figure supplement 1B–D**), our morphological data point to a less
177 elaborated basal dendrite complexity in mutant LVPNs. In particular, the basal DCI
178 was significantly reduced in *Nr2f1cKO* compared to *Ctrl* LVPNs (**Figure 2D–E)**, as a
179 result of a reduced number of primary dendrites, branching points and terminal tips
180 (**Figure 2F–H**). Overall, our data indicate that loss of Nr2f1 function affects the
181 complexity of basal dendrite geometry in LVPNs at early postnatal stages.

182

183 **Reduced conformation and plasticity properties of the axon initial segment in**
184 **mutant *Nr2f1* LVPNs**

185 Intrinsic excitability and dendritic changes are often accompanied by variations in
186 structural properties of the axon initial segment (AIS), a specialized structure
187 playing a pivotal role in integration of synaptic inputs and action potential initiation
188 (Yamada and Kuba, 2016, Kole and Stuart, 2012). It has been reported that distinct
189 AIS features, such as length and/or location relative to the soma, are crucial for the
190 homeostatic control of neuronal excitability in layer V pyramidal neurons (Hamada
191 et al., 2016). The observed reduction of basal dendrite complexity, sag response and
192 the presence of more depolarized *Vrest* together with the lack of effect on the input-
193 output relationship (**Figure 1**; **Figure 1 - figure supplement 1)**, led us to
194 hypothesize that structural homeostatic scaling of the AIS could occur in *Nr2f1cKO*
195 LVPNs. This could act as a potential mechanism stabilizing action potential
196 generation, as observed in previous studies (Hamada et al., 2016, Gulledge and
197 Bravo, 2016). To test this hypothesis, we analyzed AIS structure of P7 LVPNs *Ctrl*
198 and *Nr2f1cKO* somatosensory cortices employing the cytoskeletal scaffolding protein
199 Ankyrin G – a widely used marker of the AIS – (Kordeli et al., 1995, Zhou et al., 1998),
200 together with CTIP2, a *bona fide* layer V marker (Arlotta et al., 2005), and NeuN, a
201 neuronal marker labelling the soma (**Figure 3**). Notably, we found a significantly
202 reduced length and diameter of the Ankyrin-positive AIS in *Nr2f1cKO* compared to
203 *Ctrl* LVPNs (**Figure 3A–C**), indicating that altered intrinsic excitability and structural
204 dendritic changes of mutant LVPNs are accompanied with structural changes in AIS
205 conformation (Grubb and Burrone, 2010, Wefelmeyer et al., 2016, Kuba et al., 2010,
206 Kuba, 2010). Decreased length and diameter were maintained in P21 LVPNs
207 (**Figure 3D-F**), suggesting that altered AIS structure observed at P7 is not the result
208 of a delayed neuronal maturation.

209 Finally, to assess whether *Nr2f1*-deficient LVPNs would still respond to
210 depolarizing input despite their reduced AIS length and diameter, we performed
211 chronic depolarization treatment (+7mM of KCl for 6h) in acute brain slices of *Ctrl*
212 and *Nr2f1cKO* P7 pups (Dumitrescu et al., 2016). While the depolarization treatment
213 reduced, as expected, the relative AIS length of *Ctrl* LVPNs, no significant changes
214 were observed in AIS size between depolarization and control treatment of *Nr2f1*-

215 deficient LVPNs (**Figure 3G, H**). These data unveil that mutant LVPNs are not able to
216 undergo AIS plasticity upon increase in network activity.
217
218 **Altered expression of ion channels and glutamate receptors in postnatal**
219 **cortices of *Nr2f1cKO* mutants.**
220 Neuronal intrinsic excitability and AIS functionality of immature neurons are
221 primarily determined by the expression, subcellular distribution and biophysical
222 properties of K^+, Na^+ and Ca^{2+} channels. We next conceived that alterations in
223 intrinsic excitability of *Nr2f1*-deficient LVPNs might correlate with abnormal
224 expression of voltage gated ion channels. To test this hypothesis, we performed RT-
225 qPCR for an extensive list of K^+, Na^+ and Ca^{2+} channels specifically expressed in deep
226 layers, from P7 *Ctrl* and *Nr2f1cKO* whole cortical lysates (**Figure 4; Figure 4 - figure**
227 **supplement 1)**. Out of 33 ion channels that we could successfully test, we found a
228 significant reduction in the *mRNA* levels of only *Hcn1*, *Kcnab1*, *Kcnk2*, *Cacna2d1*,
229 *Gria3* and *Grin1* in *Nr2f1cKO* when compared to *Ctrl* brains (**Figure 4A ; Figure 4 -**
230 **figure supplement 1**). Changes in expression levels of some relevant voltage-gated
231 ion channels were subsequently confirmed through western blot analysis in *Ctrl* and
232 *Nr2f1cKO* brain lysates. Notably, we found significantly decreased protein levels of
233 the hyperpolarization-activated cation channel HCN1 (Shah, 2014) in *Nr2f1cKO*
234 when compared to *Ctrl* cortices (**Figure 4B**). Moreover, double staining of HCN1 and
235 CTIP2 on P7 cortical sections (**Figure 4C**) confirmed decreased HCN1 protein signal
236 intensity in CTIP2-expressing LVPNs (**Figure 4D**), supporting reduction of HCN1
237 protein in layer V somata of *Nr2f1cKO* mutant brains.
238 Finally, we investigated whether voltage gated ion channels were directly
239 regulated by Nr2f1. To address this, we searched for evolutionary conserved binding
240 sites for Nr2f1 on the group of differentially-expressed genes using the ECR browser
241 tool (Loots and Ovcharenko, 2007, Ovcharenko et al., 2004). We identified conserved
242 binding sites for Nr2f1 at 25kb of the 5'UTR of *Hcn1*, 3kb of the 5'UTR of *Kcnab1* and
243 proximal to the 5'UTR of *Kcnd2* loci (**Figure 4E**). To experimentally test direct
244 regulation of the expression of these ion channels by Nr2f1, we performed
245 chromatin immunoprecipitation (ChIP) assay on whole newborn *Ctrl* cortices.
246 Among all the consensus sites identified, binding of Nr2f1 by ChIP unveiled
247 reproducible binding and significant enrichment only on the *Hcn1* genomic sequence

248 (**Figure 4F**).

249 These findings on the molecular landscape of the somatosensory cortex
250 indicate that while expression levels of several ion channels might be modulated by
251 Nr2f1 during cortical development, only few ion channels seem to be directly
252 controlled by Nr2f1. We identified *Hcn1* gene as a direct target, whose protein
253 product is known to modulate voltage sag and intrinsic excitability (Brager et al.,
254 2012, Fan et al., 2016), in agreement with our electrophysiological data (**Figure 1**).
255

256 **Alterations in $Ca2^{+}$ burst and synchronous activity in early postnatal *Nr2f1*-**
257 **deficient cortices**.

258 We next hypothesized that electrophysiological, morphological and structural
259 alterations together with decreased HCN1 expression levels could translate into
260 altered patterns of spontaneous cortical network activity (Klueva et al., 2012). To
261 test this premise, we set up time lapse Ca^{2+} imaging in acute horizontal cortical slices
262 of *Ctrl* and *Nr2f1cKO* P1 and P4 mouse pups (**Figure 5**). These two stages represent
263 critical timepoints of early cortical circuit establishment that precede sensory arrival
264 from thalamic inputs (Corlew et al., 2004). The time course of Ca^{2+} activity from
265 individual cells was quantified through moving average and further filtered for
266 bursting cells, thus excluding inactive neurons (**Figure 5A**). When we analyzed the
267 Ca^{2+} burst frequency (**Figure 5B)**, we observed an overall increase from P1 to P4, in
268 accordance with previous studies (Corlew et al., 2004). To assess the level of cortical
269 network maturation, we measured the correlation index of Ca^{2+} bursts for each
270 experiment, as a way to assess synchronization, by quantifying the number of bursts
271 across cells in a 3s sliding window (Kirkby et al., 2013). As expected, we observed
272 increased correlation with network maturation progression (**Figure 5C**).

273 Next, we determined whether loss of Nr2f1 function would affect Ca^{2+} burst
274 frequency and synchronization in the developing P1 and P4 cortices. Interestingly,
275 we observed that Ca^{2+} burst frequency was higher in *Nr2f1cKO* brain slices than in
276 the corresponding *Ctrl* cohorts at P1, but not at P4 (**Figure 5B**). Moreover, by
277 comparing the Ca^{2+} burst synchronization events between *Ctrl* and *Nr2f1cKO* brains,
278 we observed no differences at P1, but instead a decreased synchronization rate in P4
279 mutant brains (**Figure 5C**). Since synchronization increases with time, these results
280 suggest an impaired maturation of network complexity in mutant brains. Next, we

281 pooled experiments by age and genotype and performed a hierarchical clustering
282 using burst frequency and synchronization (**Figure 5D**). The findings indicate that
283 network maturation might be the main factor contributing to differences in *Ctrl* and
284 *Nr2f1cKO* brains since hierarchical clustering provided stronger evidence of data
285 clustering at P1 than at P4.
286 Our previous data on ion channel transcript differences between the two
287 genotypes support alterations in the endogenous activity of developing sensory
288 areas, most probably affecting the overall frequency at early stages and leading to an
289 asynchronized network at later stages. Taken together, our data indicate that
290 spontaneous network activity and synchronization patterns are altered upon loss of
291 Nr2f1 early after birth, thus deviating from a normal developmental trajectory
292 during neocortical development.
293
294 **Impaired intrinsic network and bursting activity in cultured *Nr2f1*-deficient**
295 **cortical neurons.**
296 A recent study shows that subcortical spontaneous activity in the embryonic and
297 postnatal brain contributes to the formation of the S1 cortical map (Anton-Bolanos
298 et al., 2019). We thus aimed to explore whether altered neuronal Ca^{2+} frequency and
299 synchronization events would result exclusively from changes in spontaneous
300 cortical activity intrinsic to the S1 cortex, as opposed to changes in inputs external to
301 S1. To this purpose, we isolated somatosensory cortices from E18.5 *Ctrl* and
302 *Nr2f1cKO* brains, respectively, and cultured the dissociated neurons onto coated
303 multielectrode arrays (MEA). This allowed us to assess network activity during
304 cortical network assembly in an *in vitro Ctrl* and *Nr2f1cKO* embryo-derived model in
305 the absence of extracortical inputs. By recording the firing frequency, number of
306 bursts and their duration at different time points (days in vitro, DIV), we monitored
307 the state of excitability of the neural network (**Figure 6; Figure 6 – figure**
308 **supplement 1**). Since network maturation correlates with the expression of
309 synchronized events, cross correlation probability between the firing at individual
310 recording sites was used as a quantification parameter of network development *in*
311 *vitro* (Gavello et al., 2012, Gavello et al., 2018).
312 Our recordings on primary cultured neuronal networks failed to display any
313 spontaneous electrical activity before 6DIV (*data not shown*). This prompted us to

314 compare the average firing frequency of the earliest events taking place at 9DIV
315 (**Figure 6A**). We first observed that while *Ctrl* cortical network fired on average at
316 0.51±0.04 Hz, *Nr2f1cKO* activity was significantly lower (0.30±0.04 Hz) (**Figure 6A,**
317 **B**). However, despite observing a comparable average number of bursts in *Ctrl* and
318 *Nr2f1cKO* brains (**Figure 6C**), these bursting events were significantly longer in
319 mutant than *Ctrl* neurons (**Figure 6D**), while firing activity was more clustered into
320 bursts in mutant *neurons* (**Figure 6E**). Notably, the firing synchronization index
321 resulted higher in *Nr2f1cKO* than in *Ctrl* neuronal networks (**Figure 6F**). Hence, loss
322 of *Nr2f1* leads to an overall reduced firing frequency, but also to an increased
323 tendency of firing as bursts rather than isolated spikes in 9DIV-derived cortical
324 neurons. Together with the presence of longer burst duration and increased
325 network synchronization, these data point to an involvement of *Nr2f1* in the control
326 of processes that govern neuronal network excitability.

327 Next, we assessed the rate of firing activity, number of bursts and burst
328 duration in *Ctrl* and *Nr2f1cKO* 15DIV neuronal cultures. At this stage, we observed
329 that the firing frequency of *Ctrl* cortical networks reached a maximum value, which
330 then decreased at 20DIV (*data not shown*). We therefore compared firing parameters
331 measured at 15DIV with those measured at 9DIV to assess whether network
332 maturation was affected *in vitro*. Interestingly, we observed that from 9DIV to
333 15DIV, the developmental increase in firing activity and in the number of bursts of
334 somatosensory neurons was reduced in *Nr2f1cKO* neuronal networks (**Figure 6 –**
335 **figure supplement 1A-C**), together with the burst duration, which was significantly
336 decreased in mutant neurons at 15DIV compared to 9DIV (**Figure 6 – figure**
337 **supplement 1D**). Finally, the percentage of spikes within bursts was also
338 diminished in *Nr2f1cKO* (**Figure 6 – figure supplement 1E**), in accordance with
339 impaired network synchronization, which resulted lower in *Nr2f1cKO* than in *Ctrl*
340 neurons (**Figure 6 – figure supplement 1F**). Taken together, these results indicate
341 that spontaneous network activity generated within the neocortex in the absence of
342 extracortical inputs is affected upon loss of cortical *Nr2f1*. This suggests that *Nr2f1*
343 might be directly or indirectly involved in modulating intrinsic spontaneous network
344 activity in the developing somatosensory cortex.

DISCUSSION

Our work reveals that the area patterning gene *Nr2f1* can influence the emergence of spontaneous activity and intrinsic excitability within the immature somatosensory cortex during early postnatal development. These findings reinforce the role for *Nr2f1* in somatosensory area development, as previously reported (Alfano et al., 2014, Armentano et al., 2007). More importantly, they provide, to our knowledge, first experimental proof for a patterning gene involved in cortical area and cell-type specification that directly determines early patterns of spontaneous network activity intrinsic to the immature cortex. Developmental spontaneous activity has already been described to ultimately influence the formation of long range circuits (Tritsch et al., 2007, Blankenship et al., 2011, Yamamoto and Lopez-Bendito, 2012, Schneggenburger and Rosenmund, 2015, Anton-Bolanos et al., 2019) as well as showing a regionalized pattern in the cortex (Corlew et al., 2004, Uhlen et al., 2015). However, in this study, genetic manipulation targeting exclusively cortical neurons allows to investigate the specific contribution of patterning genes to intrinsic network activity within the neocortex. Our findings provide a primary link between intrinsic genetic determination and spontaneous cortical activity through the regulation of voltage-gated ion channels in pyramidal glutamatergic neurons. Moreover, we also show that the hyperpolarization-activated cation channel HCN1 – known to contribute to intrinsic neural excitability and spontaneous rhythmic activity in the brain (Shah, 2014)– is a potential direct effector of electrical activity regulated by *Nr2f1* during establishment of neuronal synchronicity in the developing neocortex.

Determinants of spontaneous network activity controlled by patterning genes during cortical area identity specification

Normal developmental trajectories in the cerebral cortex are characterized by a sequential process of spontaneous activity patterns in immature networks. In the mouse neocortex, large plateaus of synchronized network activity at birth are followed by early network oscillations and large depolarization potentials along the first postnatal week (Allene et al., 2008, Allene and Cossart, 2010). Multiple aspects that relate to intrinsically regulated maturation of pyramidal neurons might influence the developmental sequence of cortical network activity. Our data provide

a novel characterization at the electrophysiological and molecular levels of intrinsic excitability features directly or indirectly regulated by the transcriptional regulator *Nr2f1* during the first postnatal week. Our evaluation of how *Nr2f1* expression influences the molecular determinants relevant for early neuronal network activity is corroborated by previous transcriptome analyses, in which *Nr2f1* loss in post-mitotic cortical cells regulate the expression of several activity related genes, such as *Chrna7, Kcnq3, Kcnlp4, Robo1* and *Sv2b* (Alfano et al., 2014). However, the direct impact of these candidates on immature cortical neuron activity still remains to be investigated.

Other recent studies also highlighted the role of cell intrinsic and pre-synaptic factors in determining cortical network development with potential long-term effects (Boillot et al., 2016, Murase et al., 2016). In addition, a recent report has shown that the transcription factor Tbr1, known to regulate cortical layer identity, alters the intrinsic excitability of neocortical neurons, by regulating HCN1 transcription in neonates and increasing sag response in layer VI (Fazel Darbandi et al., 2018). As Tbr1 is also a key factor for cortical development, it is presumably regulating spontaneous network activity intrinsic to the neocortex during early developmental stages, but this still remains to be addressed. Hence, our work sets the first evidence that spontaneous network activity intrinsic to the cortex is regulated during early neocortical development by a key area patterning transcriptional regulator.

Within immature cortical networks, the earliest patterns of correlated spontaneous activity – e.g. synchronous plateau assemblies – are thought to arise from voltage-gated intrinsic conductance and gap junction coupling (Pearson et al., 2004, Roerig and Feller, 2000, Blankenship et al., 2011, Cho and Choi, 2012). Our work features intrinsic excitability – more precisely, intrinsic bioelectrical properties of neural membranes – as an important component of neocortical development, most likely contributing to the abnormal cortical patterning defects displayed in *Nr2f1* mutants. In this context, it is important to note that *Nr2f1* loss also affects the expression of many cell-adhesion related genes *(i. e., Cdh4, Cdh11, Cdh12, Fat3,* and *Ncam2*) (Alfano et al., 2014), which could in turn affect gap-junction functionality. Interestingly, intrinsic bioelectrical membrane properties prominently determine the occurrence of membrane potential spikes before gap-junction

411 coupling takes place (Allene and Cossart, 2010). Hence, it is tempting to speculate
412 that even earlier forms of activity within the embryonic brain could be responsible
413 for the abnormal area specification observed in the absence of *Nr2f1* (Armentano et
414 al., 2007; Alfano et al., 2014).
415
416 **Nr2f1-dependent *versus* homeostatic changes in intrinsic neural excitability.**
417 Our functional analysis indicates that an abnormally differentiating somatosensory
418 area displays increased spontaneous network activity at P1 followed by decreased
419 synchronization within immature neurons at P4. Principal factors for increased
420 excitability of neural network might be the more depolarized resting membrane
421 potential of pyramidal glutamatergic neurons, which might contribute to the higher
422 frequency of Ca^{2+}-events observed at P1. Alternatively, a decreased expression of
423 voltage sag (I_h) could lead to opposite changes in membrane excitability, which are
424 strongly age-dependent (Bender and Baram, 2008, Magee, 1998, Williams and
425 Stuart, 2000, Williams and Stuart, 2003, Berger et al., 2001, Poolos et al., 2002,
426 Poolos et al., 2006, Wang et al., 2003, Fan et al., 2005, van Welie et al., 2006, Brager
427 and Johnston, 2007, Chen et al., 2001). Multiple membrane ion channels, which
428 expression is altered in pyramidal neurons upon loss of *Nr2f1* function, could
429 contribute to the increase in resting membrane potential in immature neurons, a
430 property of pyramidal neurons that matures during the two first weeks after birth.
431 In our *ex vivo* electrophysiological analysis, some membrane properties of *Nr2f1cKO*
432 LVPNs, such as *Vrest* and *APamp*, resemble those of less mature neurons. However,
433 other electrophysiological parameters, e.g. R*in*, do not change and therefore are not
434 in agreement with a delayed maturation in intrinsic properties. In addition, our
435 analysis on AIS homeostatic plasticity at P21 does not point to a maturation defect in
436 individual neurons, but rather to a stabilized state of abnormal intrinsic excitability
437 leading to decreased dendritic complexity and AIS plasticity, as a possible
438 homeostatic/compensatory mechanism.
439 Our work using *ex vivo* electrophysiology together with molecular analysis
440 strongly suggest that *Nr2f1* directly regulates HCN1 expression. It is complex to
441 precisely dissect changes in membrane-ion channels, priming the start of abnormal
442 network excitability, from those that are concomitantly changing by intrinsic or
443 homeostatic plasticity. Since *Nr2f1* directly regulates HCN1 transcription, we

propose that decreased HCN1 levels could act as initiator of the deregulation in intrinsic as well as network activity observed in mutant cortices. Therefore, it is conceivable that the alterations in expression levels we observed in other voltage-gated ion channels at P5–P8 are the product of additional network-activity-driven compensatory mechanisms occurring after P1 or P4. In other words, we hypothesize that changes in ion-channel expression of pyramidal glutamatergic neurons at P5–P8 are due to homeostatic and/or intrinsic plasticity changes following earlier alterations in overall network activity state. For example, experimental evidence from the developing hippocampus suggests that the induction of increased bursting activity and seizures alters persistently HCN channel expression and voltage-dependence of I_h current (Arnold et al., 2019, Chen et al., 2001). Acting as a direct transcriptional regulator of HCN1, we propose that Nr2f1 could influence spontaneous network activity intrinsic to the somatosensory cortex by contributing to the establishment of the bioelectrical state of glutamatergic neurons at the time point, and probably before, the start of cortical network formation. Moreover, intrinsic pacemaker properties through HCN1 expression has been hypothesized to generate and drive distinct synchronized activity patterns in immature networks (Luhmann et al., 2016).

Importantly, genetic or pharmacological dysfunction in HCN channels in mice results in behavioral phenotypes associated to somatosensory-motor coordination, e.g. reduced forelimb reaching accuracy and atypical movements during a single-pellet skill reaching task (Boychuk et al., 2017). This is very analogous to the behavioral phenotypes displayed by *Nr2f1cKO* mice (Tomassy et al., 2010) and symptoms of NR2F1 haploinsufficient patients (Bosch et al., 2014, Chen et al., 2016), suggesting that Nr2f1 might influence cortical maps involving voluntary movements by allowing coordinated skilled behavior *via* the action of HCN1.

Together with the cellular and molecular role of Nr2f1 during intrinsic area patterning, this study has unraveled a key and novel functional role of this transcriptional regulator in cortical intrinsic excitability and spontaneous activity that might affect axonal connectivity and circuit formation necessary for behavioral abnormalities described in mice (Contesse et al., 2019, Flore et al., 2017, Tomassy et al., 2010) and, possibly, in humans (Chen et al., 2016, Bosch et al., 2016), reviewed in (Bertacchi et al., 2019).

ACKNOWLEDGMENTS:

We thank Dr. Marteen Kole and Dr. Nathalie Dehorter for critical reading of the manuscript and members of the Studer, Leinekugel and Frick laboratories for stimulating discussions. We also thank the iBV PRISM Microscopy facility and the Bordeaux Imaging Center (BIC) for their regular support. This work was supported by an ANR (Agence National de la Recherche) grant # ANR-13-BSV4-0011-01 to M.S. and X.L, by the "Fondation Recherche Médicale; Equipe FRM 2015 grant #DEQ20150331750; by an ''Investments for the Future'' LabEx SIGNALIFE (grant ANR-11- LABX-0028-01) to M.S. and by the "Initiative d´Excellence (IdEx) de l´Université de Bordeaux" fellowship to I.D.P.

Corresponding author statement:

The corresponding author declares non-financial competing interest on behalf of all authors.

498 **MATERIALS & METHODS**

499 **Mice**

500 Nr2f1/COUP-TFI*fl/fl* mice were crossed to *Emx1-Cre* mice to inactivate *COUP-*
501 *TFI/Nr2f1* exclusively in cortical progenitors and their progeny (Armentano et al.,
502 2007). These mice are denominated *Nr2f1cKO* throughout the text. Mice were
503 genotyped as previously described (Armentano et al., 2007). For P21 studies,
504 Control (*Nr2f1 fl/fl)* and mutant *Nr2f1cKO* mice were crossed to *Thy1-eYFP-H* mice to
505 specifically mark LVPNs, as previously reported (Harb et al., 2016). Midday of the
506 day of the vaginal plug was considered as embryonic day 0.5 (E0.5). Control (*Nr2f1*
507 *fl/fl)* and mutant *Nr2f1cKO* mice were predominantly bred in a C57BL6 background.
508 Both male and female embryos and pups were used in this study. All mouse
509 experiments were conducted according to national and international guidelines,
510 with authorization #15349 and 15350 by the French Ministry of Education,
511 Research and Innovation (MESRI) and upon request of the local ethics committee –
512 CIEPAL NCE/2019-548 (Nice) and CEEA50 (Bordeaux), and in accordance with the
513 guidelines established by the Italian National Council on Animal Care and approved
514 by the local Animal Care Committee of University of Turin (Authorization DGSAF
515 0011710-P-26/07/2017).

516

517 ***Ex vivo* electrophysiology and analysis**

518 Mouse pups at postnatal stage (P)5–P8 were decapitated and brains were placed on
519 ice-cold modified artificial cerebrospinal fluid (aCSF) containing (in mM): 87 NaCl,
520 25 $NaHCO_3$, 5 Glucose, 65 Sucrose, 2.5 KCl, 1.25 NaH_2PO_4, 0.5 $CaCl_2$, 7 $MgCl_2$
521 saturated with 95% CO_2 and 5% O_2. Coronal slices of 300µm were cut in a vibratome
522 (Vibratome 300 Plus, Sectioning Systems) and gently transferred to room
523 temperature aCSF containing (in mM): 125 NaCl, 25 $NaHCO_3$, 25 Glucose, 2.5 KCl,
524 1.25 NaH_2PO_4, 2 $CaCl_2$, 1 $MgCl_2$ saturated with 95% CO_2 and 5% O_2 (pH 7.4) .

525 Current-clamp recordings were performed at 32-34°C using a potassium-
526 gluconate based intracellular solution containing (in mM): 120 K-Gluconate, 20
527 HEPES, 0.5 EGTA, 15 KCl, 4 MgATP and 0.3 NaGTP (pH 7.4) and osmolarity set to 299
528 mosmol l^{-1}. Biocytin (1.5 – 2 mg ml^{-1}) was added to the intracellular solution for
529 post-hoc immunohistochemistry. Neurons were visualized with an upright
530 microscope (Zeiss Axio Examiner D1) equipped with an Evolve 512 EMCCD Camera

531 (Photometrics) using a 63X/1.0nA water-immersion objective (Zeiss) and infrared
532 DodT contrast imaging. Recording pipettes (6-10MΩ) were pulled from borosilicate
533 glass using a Narishige P-10 puller. Data was acquired using a Dagan BVC-700A
534 Amplifier, low-pass filtered at 3kHz and sampled at 20kHz with ITC16 (Instrutech)
535 and AxoGraph X software. Membrane voltage was recorded in the bridge mode. To
536 determine the excitability of pyramidal neurons, we performed 800ms square
537 current steps of 10pA from -100pA to +150pA. The rheobase was defined as the
538 minimum somatic current required to elicit an action potential (AP) from the resting
539 membrane potential of the neuron. Input resistance was calculated from voltage
540 responses to -20pA. Threshold potential was defined as dV/dt = 10mV/ms. Inter-
541 spike interval (ISI) was calculated as the difference between first and second AP at
542 the minimal current to elicit >2AP. The amplitude of action potentials was measured
543 from both restingmembrane potential to peak and also from spike threshold (see
544 Table 1). Action potential width was measured at half of the maximum amplitude
545 (APhalf-width or AP*h-w*). Voltage sag was calculated as the difference between
546 steady-state and minimum voltage transient resulting from hyperpolarizing (-
547 150pA) current injections.
548
549 ***Post-hoc* immunofluorescence**
550 Brain slices were fixed overnight at 4°C with 4% paraformaldehyde in 0.1M
551 phosphate buffer (PB) pH7.4. The following day slices were washed 3 x 10 min with
552 0.1M PB and incubated overnight at 4°C with Alexa-Flour®-conjugated streptavidin
553 diluted 1:500 in 0.1M PB. The following day slices were washed 3 x 10 min with
554 0.1M PB, stained with DAPI and mounted with Mowiol.
555
556 **KCl *ex vivo* depolarization assay**
557 *Ctrl* and *Nr2f1cKO* P7 mice were sacrificed by decapitation and brains dissected into
558 ice-cold aCSF saturated with 95% O_2 and 5% CO_2. 300µm-thick slices were produced
559 by vibratome sectioning and then transferred into homemade floating nests
560 immersed into aCSF, kept at room temperature and constantly saturated with 95%
561 O_2 and 5% CO_2. After 15 minutes of acclimatization, slices from both genotypes were
562 split into two groups: an untreated group (**- KCl**) and an experimental group (**+ KCl**).
563 KCl were added to the aCSF of the experimental group whereas control slices were

564 kept in normal aCSF. After an incubation time of 6 hours(Dumitrescu et al., 2016),
565 slices were washed for 15 minutes in aCSF and then processed for
566 immunofluorescence (IF), as described below.
567
568 **Histology and immunohistochemistry of mouse perinatal cortices**
569 Perinatal mice (P7-8) were anesthetized by using a mixture of Tiletamine-
570 Zolazepam-Xylazine-Buprenorphine (TZXB) and intracardially perfused with
571 Phosphate Buffer Saline (PBS) followed by 4% paraformaldehyde (PFA) in PBS. Then,
572 brains were dissected and post-fixed for 4h at 4°C in 4% PFA and then vibratome-
573 sectioned to obtain 100 m thick, coronal or sagittal floating sections. Overnight
574 (ON) incubation at 4°C in a solution of 0.5% Triton X-100, 3% BSA, 10% Goat Serum
575 in PBS was performed to permeabilize the sections and reduce non-specific binding
576 of the antibodies. For immunofluorescence (IF), sections were incubated for two ONs
577 at 4°C with indicated primary antibodies in a solution of 0.5% Triton X-100, 10%
578 Goat Serum in PBS and then ON at 4°C with relative secondary antibodies (see **Key**
579 **resource table**) and HOECHST diluted in PBS. Regarding the HCN1 IF, brains were
580 briefly post-fixed for 30 minutes (min) at 4°C in 4% PFA and then immediately
581 sectioned with the vibratome to obtain 50μm thick coronal floating sections.
582 Permeabilization-blocking step was reduced to 2h, primary antibody incubation to
583 one ON and secondary antibody and HOECHST incubation to 2h. Sections were then
584 transferred on superfrost plus slides (ThermoScientific), let dry for 30min to 1h and
585 finally mounted with Mowiol mounting medium.
586
587 **Microscopy and image analysis**
588 Imaging was performed using a Zeiss 710 confocal microscope equipped with a
589 405nm diode, an argon ion, a 561nm DPSS and a 647 HeNe lasers. Z-stacks of fixed
590 cortical sections were imaged using a LD-LCI Plan-Apo 25x/0.8 NA or a LD Plan-Apo
591 63x/1.4 NA oil immersion lenses. Images from IF experiments were analyzed by
592 using Fiji-ImageJ Software (Schindelin et al., 2012): cell counter plug-in was used to
593 assess the number of cells expressing specific proteins, while measurement tools
594 were used to determine signal intensity or Axonal Initial Segment (AIS) features
595 such as length and distance from the soma. For the AIS average diameter
596 measurement, we took advantage of IMARIS software's tool filament tracer. AISs

597 were semi-automatically reconstructed and an average diameter automatically
598 measured for every AIS individually.
599 Morphological characterization of biocytin filled layer V pyramidal neurons
600 (LVPNs) was analyzed by using IMARIS software. Cell arborization was
601 reconstructed in a semi-automatic manner, via the filament tracer module.
602 Automatic length measuring tool was used to calculate the total dendritic length and
603 the basal dendritic length. Branching points, branching point orders and tips were
604 manually quantified for both basal and apical dendrites, as well as primary and
605 lateral dendrites. The branch tip order is an integer value equivalent to the number
606 of branching points a dendrite undergoes from its somatic origin to the terminal tip
607 (see also Figure 2D for a graphic representation). Primary dendrites were identified
608 as directly originating from the soma, lateral dendrites were categorized as
609 originating from and perpendicular to the apical dendrite whereas total and basal
610 branch tips were identified as the terminal ends of primary dendrites including or
611 excluding the apical dendrite arborization respectively.
612 The basal Dendritic Complexity Index (bDCI) was calculated as follows:

$$bDCI = \frac{\sum \text{basal branch tip orders+basal branch tips}}{\text{Primary dendrites}} \text{Basal Arbor Length}$$

613 An automatic detection of Sholl intersections was used to compute Sholl profiles for
614 every individual cells. Sholl intersections were identified as the number of dendrite
615 intersections for concentric spheres of increasing radius and having as a center the
616 centroid of the cell body. Distance between radii was set at 10μm.
617
618 **RNA extraction and cDNA synthesis**
619 RNA for reverse transcriptase–PCRs (RT–PCRs) was extracted from P0 and P7
620 dissected neocortices separated from meninges of *Ctrl* and *Nr2f1cKO* mice (n=3) and
621 was extracted using the RNeasy Mini kit (Qiagen) following manufacturer's
622 instructions. We synthetized cDNA from 1μg of total RNA using Superscript III First-
623 Strand Synthesis System for RT–PCR (Invitrogen) following manufacturer's
624 instructions.
625
626 **qPCR RNA/cDNA quantification**
627 qPCRs on cDNA was performed using KAPA Sybr Fast (Kapa Biosystems) according

628 to manufacturer's instructions. Samples were run on a LigthCycler II 480 (Roche)
629 and the following primers were used: GAPDH Fw: GTATGACTGCACTCACGGCAAA.
630 Rev: TTCCCATTCTCGGCCTTG; Cacna1A Fw: GGGCCCAAGAGATGTTCCAG. Rev:
631 TCCACAGACTGGGAGTTGGG; Cacna1B Fw: CACGCAGAGGACCCACGATG. Rev:
632 CATCACAGCCAGTGTTCCTG; Cacna1G Fw: TCAGCTGCCTGTCAACTCCC. Rev:
633 CCCATCACCATCCACACTGG; Cacna1H Fw: ACCTACACAGGCCCGGTCAC. Rev:
634 ATGGGACCTGGAAGGAGGTG; Cacna2D1 Fw: CAGGGAGGGCACTGATCTTC. Rev:
635 TTGATAGTGACGGGCGAAGG; Cacna2D3 Fw: TTAGGTGTGGCGCTCTCCAG. Rev:
636 GCCAAGGACACGTCAGGATG; Hcn1 Fw: TGCCACAGCTTTGATCCAGT. Rev:
637 GCGCATGTCAGCTGGTAACT; Kcnab1 Fw: TCCCATGGAAGAAATCGTTCG. Rev:
638 CTTCCATGATCTCCATCGCG; Kcnd2 Fw: GGGAAGCCATAGAGGCAGTG. Rev:
639 GTGGAGTTCTCTCCACACATCTG; Kcng3 Fw: CAACCGCAGTCTGGATGACC. Rev:
640 CGGTGAACCACCCTATGCAG; Kcnh1: Fw: TTAGTGCCTTTATGGGTGATCC. Rev:
641 GATGCCCTGACTCTCTCTCC; Kcnh5: Fw: CTTTCCAGACCCAGGATGCC. Rev:
642 TTGATTCACTGGAGCGCCTG; Kcnj6 Fw: AACTGACGGAGAGGAATGGG. Rev:
643 TGGGTTGGGTGAATTCTGGG; Kcnk2 Fw: ACGTGGCAGGTGGATCAGAC. Rev:
644 AGTAGGCCAGCCCAACGAG; Kcnmb4 Fw: TTGGAAAGATGAGATCGGTTCC. Rev:
645 AAGCAGTGCAGGAGAGCAATC; Kv2.1 Fw: CGTCATCGCCATCTCTCATG; Rev:
646 CAGCCCACTCTCTCACTAGCAA; Gria1 Fw: CTGGTGGTGGTGGACTGTG. Rev:
647 TGTCCATGAAGCCCAGGTTG; Gria2 Fw: ATTTGGAATGGTATGGTTGGAG. Rev:
648 AGGCTCATGAATGGCTTCGAG; Gria3 Fw: TCATTCTCACGGAGGATTCCC. Rev:
649 CACAGCAAAGCGGAAAGCAC; Gria4 Fw: CCAGAGCCTCCCTGAAGACC. Rev:
650 TGCGCGCTCTCCTCTCTTTC; Grik1 Fw: AGTTGGTCGCATGCTCTTCG. Rev:
651 CGAACCTTGATGCCCAATAC; Grik2 Fw: CTGGTGGAGAGTGCTTTGGG. Rev:
652 CCACACCCTTGCAACCCTG; Grik3 Fw: TCGCCAGATTCAGCCCTTAC. Rev:
653 GCCCATTCCAAACCAGAAGC; Grik5 Fw: GCCTGCGGTTGGTAGAGGAC. Rev:
654 TCTGCCTTCCGGTTGATGAG; Grin1 Fw: TCAGAGCACACTGTGGCTGC. Rev:
655 ATCGGCCAAAGGGACTGAAG; Grin2B Fw: GGAAGTGGGAGAGGGTGGG. Rev:
656 CAGGACACATTCGAGGCCAC. For each reaction primers were used at 0.2μM using
657 10nl of total cDNA. Each sample was corrected to the housekeeping gene GAPDH.
658

659 **Dissection and western blot of mouse perinatal cortices**

660 Postnatal pups (P7-8) were sacrificed by decapitation and fresh tissues were

661 dissected immediately after. Whole cortex samples were collected and lysed in RIPA
662 buffer (10 mM Tris-Cl (pH 8.0), 1 mM EDTA, 1% Triton X-100, 0.1% sodium
663 Deoxycholate, 0.1% SDS, 140 mM NaCl, 1 mM PMSF) implemented with cOmplete
664 protease inhibitors (Roche). Protein quantity was then measured with the Pierce
665 BCA protein assay KIT (ThermoScientific). Equal amounts of proteins from tissue
666 lysates were resolved by reducing SDS-PAGE, transferred to PolyVinylidene
667 DiFluoride (PVDF) membrane and incubated with the indicated antibodies (see
668 supplementary Table 2). Immunoblots were developed using ECL Prime western
669 blotting detection reagent (GE Healthcare). Signals were normalized on actin signal
670 intensity.
671
672 **Chromatin Immuno-Precipitation (ChIP)**
673 The ChIP protocol was modified from Kuo and Allis 1999 (Methods), using protein
674 sepharose-A resin (SIGMA), prepared by washing in PBS and equilibration buffer
675 (HEPES pH7.4 20mM, EDTA 1mM, NaCl 150mM, Triton 0.8%, SDS 0.1% PMSF
676 10mg/ml). For each experiment (n=3), we dissected necortices of 8 mice at P0 in ice
677 cold HBSS and washed in DMEM. Samples were crosslinked in 0.9 formaldehyde for
678 10' and blocked adding 1.1ml of glycine 1.25M for 5'. We washed samples in wash
679 buffer (HEPES pH 7.4 20 mM, NaCl 150mM, Glycine 0.125M, PMSF 10mg/ml) and
680 isolated nuclei in Lysis buffer (HEPES pH 7.4 20mM, NaCl 150mM, Glycine 0.125M,
681 SDS 1% PMSF 10mg/ml). Nuclei were collected (2200 rcf for 5' spin) and sonicated
682 in 1.2 ml Sonication Buffer (HEPES pH 7.4 20mM, NaCl 150mM, Glycine 0.125M, SDS
683 0.4% PMSF 10mg/ml) 6 times for 5 seconds at 10μm amplitude. DNA fragments
684 were separated from cellular debris by spinning at 14000rcf for 10' and
685 recuperating the surnatant, fragmentation quality was evaluated by gel
686 electrophoresis post-hoc. DNA fragments where split in 3x300 μl samples and
687 precleared with resin Slurry solution (resin/equilibration buffer, 50/50 volume),
688 adding 50ul of Slurry to each and incubating for 1h at 4°C. Surnatant was kept after
689 spinning at 800 rcf for 2' at +4°C and were incubated overnight at +4°C with 3μg of
690 dedicated antibodies: Nr2f1 antibody (Thermo Fisher PA5-21611), GFP antibody
691 (Abcam ab13970, for aspecific binding), no antibody. A fourth samples called Mock
692 was obtained using a blank volume of Sonication buffer. We added 50μl of Slurry to
693 each sample and incubated 3h at +4°C and washed samples 4 times in ice cold

694 Washing buffer A (HEPES pH 7.4 20 mM, NaCl 150mM, Triton 100 1%, SDS 0.1%
695 PMSF 10mg/ml), 4 times in ice cold Washing buffer B (Tris pH 8.0 20mM, EDTA 1
696 mM, LiCl 250mM, NP-40 0.5%, Na-Deoxycholate 0.5%, PMSF 10mg/ml) and 2 times
697 with TE buffer (Tris HCl pH 8.0 20mM, EDTA 1mM, PMSF 10mg/ml). We eluted DNA
698 fragments denaturating antibodies adding 300µl of Elution buffer (NaHCO3 50mM,
699 1% SDS) and incubating in rotation 1h at RT. An Input samples was created here
700 mixing 300µl of Elution buffer to 10µl of the supernatant from the first washing of
701 the no-antibody sample. We separated the fragment from the resin ant antibodies
702 spinning at 8000 rcf for 2' and saving the supernatant, twice. Next, we reversed
703 crosslinks adding 12µl of NaCl 5M and incubating overnight at +65°C. RNA was
704 removed by adding 1µl of RNAse-A 10mg/ml and incubated for 30' at +37°C; the
705 reaction was blocked adding 6µl of EDTA 0.5M. Remaining proteins were digested
706 adding 12µl of Tris HCl pH 8.0 and 1µl of proteinase K 10mg/ml for 1-2h at +45°C.
707 Finally, samples were purified by phenol-chloroform extraction and precipitated
708 into 20µl of H_2Omq.
709
710 **qPCR of ChIP samples**
711 qPCRs on ChIP was performed using KAPA Sybr Fast (Kapa Biosystems) according to
712 manufacturer's instructions. Samples were run on a LigthCycler II 480 (Roche) and
713 the following primers were used: Nr2f1 binding site at Hcn1 locus Fw:
714 TTTCTGCTTTCCCGTGAGAGC. Rev: AGCCTAGCCTAGGAAGCCAG; Nr2f1 binding site at
715 Kcnab1 locus Fw: TGTGGTATCAGAGATGAAAGGC. Rev: AAGGGACCTCCCAGCTCTTC;
716 Nr2f1 binding site at Kcnk2 locus Fw: CCCAAAGCTGGACTTGTGTAC. Rev:
717 TTCCCCTGATCAAAATTCCATTC; Negative control (Egr1 binding site at Cacna1g
718 locus) Fw: AGCACCAGCTCAGATCACTCC. Rev: CAGAAGAAACTGTGTCAAGAGC. For
719 each reaction primers were used at 0.2µM using 0.5µl each sample. For proper
720 quantification, a calibration curve was included in the reactions using 6 sequential
721 1:10 solutions of samples obtained from amplicon extraction of PCR performed on
722 genomic DNA with each set of primers used. For every ChIP experiment the reaction
723 was carried out on 3 replicates of specific antibody, aspecific antibody, no antibody,
724 mock and input samples. The calculated concentration of every samples was
725 normalized to the input, set to 1 and we then calculated the fold change between the
726 samples with specific antibody against sample with aspecific antibody, which was

727 normalized to 1. Finally, the fold change of specific/aspecific antibody samples was
728 corrected by dividing for the fold change of specific/aspecific antibody samples
729 obtained from the negative control primers. Regarding the qPCR statistical analysis,
730 we performed paired t.test analysis correcting the P-value for multiple testing using
731 the Benjamini–Hochberg procedure, false discovery rate = 0.25. Data analysis scripts
732 were custom-prepared in R (Computing, 2018) and Matlab.
733
734 **Ca^{2+} imaging from *ex vivo* brain slices preparation and analysis.**
735 Animals were anesthetized by cold and brains were dissected in ice cold high-Mg
736 ACSF (125mM NaCl, 25mM $NaHCO_3$, 2.5mM KCl, 7mM $MgCl_2$, 2mM $CaCl_2$, 1.25mM
737 NaH_2PO_4, 10mM glucose, pH7.4) after decapitation. Horizontal 300 µm slices were
738 prepared on a Leica Vibratome 100M in ice cold High Mg ACSF under 95% O_2, 5%
739 CO_2 bubbling. Selected slices where incubated 1h at 37°C in ACSF (125mM NaCl,
740 25mM $NaHCO_3$, 2.5mM KCl, 2mM $CaCl_2$, 1.25mM NaH_2PO_4, 10mM glucose, pH7.4)
741 0.63% Oregon Green BAPTA™ (ThermoFisher O6807) in DMSO before proceeding to
742 image acquisition. Slices were loaded on a 35mm diameter petri dish with 1.3mm
743 glass bottom and immobilized with a custom nylon net. After 30 minutes of
744 equilibration in the microscope objective holder time lapse images were acquired
745 over a Spinning Disk microscope (Olympus / Andor technology) with a 40x air
746 objective, recording for 15 minutes at 150 ms intervals twice over M and S area for
747 each sample.
748 Images were automatically corrected for drifting using built-in Fiji
749 (Schindelin et al., 2012) function and cells profiles were manually defined as
750 separate ROI on a custom Matlab script. Single ROI were used to acquire BAPTA
751 fluorescence intensity as the mean of intensity within each area defined in each ROI
752 for every frame, thus resulting in single cell time series of Ca^{2+} signals. Each of the
753 these were individually corrected by moving average (Anderson, 1975) to generate a
754 constant baseline over the progressive signal loss. Actively bursting cells were
755 selected and considered for further analysis if in at least 40% of frames of an ROI fell
756 within the first quarter of maximum intensity of the ROI, thus excluding inactive and
757 fast spiking interneurons, concentrating the analysis on projection neurons. Within
758 selected timeseries, Ca bursts were detected filtering BAPTA intensity on a threshold
759 of 3 standard deviations. The bursting frequency of every selected cell was measured

760 dividing the number of bursts above threshold by the sum of intervals between each
761 burst. To evaluate coordination of activity, every selected time series in a recording
762 was vertically evaluated, counting the number of Ca bursts happening in the same 3s
763 time window across time series and normalizing by the total number of bursts
764 within the recording, thus obtaining a coordination index, which was then
765 normalized across in each image by dividing for the total number of Ca burst
766 multiplied by the total number selected time series, thus obtaining a single
767 correlation index per image. All time-lapse analysis was performed using a custom
768 Matlab script.
769
770 **MEA recordings on primary cultures and analysis of MEA activity.**
771 Cortical neurons were obtained from E18.5 *Ctrl* and *Nr2f1cKO* mouse embryos.
772 Cortices were rapidly dissected under sterile conditions, kept in cold HBSS (4ºC)
773 with high glucose, and then digested with papain (0.5 mg/ml) dissolved in HBSS plus
774 DNAse (0.1 mg/ml), as previously described (Gavello et al., 2018). Isolated cells
775 were then plated at the final density of 1200 cells/mm^2 onto the MEA (previously
776 coated with poly-DL-lysine and laminin). Cells were incubated with 1 %
777 penicillin/streptomycin, 1% glutamax, 2.5% foetal bovine serum, 2% B-27
778 supplemented neurobasal medium in a humidified 5 % CO_2 atmosphere at 37ºC.
779 Each MEA dish was covered with a fluorinated ethylene-propylene membrane (ALA
780 scientific, Westbury, NY, USA) to reduce medium evaporation and maintain sterility,
781 thus allowing repeated recordings from the same chip.
782 Multisite extracellular recordings from 60 electrodes were performed using
783 the MEA-system, purchased from Multi-Channel Systems (Reutlingen, Germany).
784 Data acquisition was controlled through MC_Rack software (Multi-Channel Systems
785 Reutlingen, Germany), setting the threshold for spike detection at -30 μV and
786 sampling at 10 kHz. Experiments were performed in a non-humidified incubator at
787 37°C and with 5% CO_2, without replacing the culture medium. Before starting the
788 experiments, cells were allowed to stabilize in the non-humified incubator for 90
789 seconds; then the spontaneous activity was recorded for 2 minutes.
790 Bursts analysis was performed using Neuroexplorer software (Nex
791 Technologies, Littleton, MA, USA) after spike sorting operations. A burst consists of a
792 group of spikes with decreasing amplitude, thus we set a threshold of at least 3

spikes and a minimum burst duration of 10ms. We set interval algorithm specifications such as maximum interval to start burst (0.17 sec) and maximum interval to end burst (0.3 sec) (Gavello et al., 2012, Gavello et al., 2018). Burst analysis was performed by monitoring the following parameters: mean frequency, number of bursts and mean burst duration. Cross correlation probability values were obtained by means of Neuroexplorer software using ± 2 s and 5 ms bin size. The number of experiments is referred to the number of MEA each of those consisted of 59 recording electrodes.

Statistical tests.

Principal component analysis (PCA) was performed on R software using Factominer and the following parameters: V*rest*, R*in*, Rheobase, V*threshold*, APamplitude, APhalf-width, latency, Sag and ISI. In PCA plots, ellipses represent the 95% confidence and the square the center of mass for each cluster. Hierarchical clustering was performed with Euclidean distance, using both average burst frequency and correlation per condition. All statistical analysis scripts were custom-prepared in R (Computing, 2018). Additional statistical analyses were also performed using Graphpad Prism7 and data are presented as mean ± s.e.m. *n* values represent biological replicates from > 3 different brains and > 3 different litters. No statistical tests were used to predetermine sample size but samples sizes were similar as reported in previous publications (Del Pino et al., 2017, Del Pino et al., 2013) or as generally employed in the field. No randomization was used. Whenever possible both genotypes were processed in parallel. *Ex vivo* electrophysiology experiments and analysis of all data were performed blind to genotype. Differences were considered significant when $P < 0.05$. Data sets were tested for normality (Kolmogorov-Smirnov) or homoscedasticity (Leven test) before performing parametric (Student t-test, one-way or 2-way ANOVA followed by Bonferroni's post-hoc test) or non-parametric tests (Welch's unequal variances t-test or Mann-Whitney test) used to determine p-values. In Figure 5B, P1 and P4 were analyzed independently, testing *Ctrl* and *Nr2f1cKO* frequency and correlation score by Welch Two-samples test.

826

827 **FIGURE LEGENDS :**

828

829 ***Figure 1. Nr2f1 deletion in the cerebral cortex results in abnormal intrinsic***
830 ***excitability of layer V pyramidal neurons.*** **A**) Layer V pyramidal neurons (LVPNs)
831 identified through fluorescent labelling for biocytin (green) and DAPI (gray) in *Ctrl*
832 (in black) and *Nr2f1cKO* (in red) somatosensory cortex display slow-adapting
833 regular spiking firing pattern. **B**) Individual factor maps (PCA) performed on
834 pyramidal neurons recorded segregate two clusters as distinct populations in *Ctrl*
835 (black) and *Nr2f1cKO* (red). **C**) Mean V*rest* is significantly increased (** *P* = 0.0013),
836 while Sag (* *P* = 0.0103) and the rheobase (*** *P* = 0.0006) are significantly
837 decreased in *Nr2f1cKO* LVPNs compared to *Ctrl* LVPNs. (N = 19 *Ctrl*, N = 28
838 *Nr2f1cKO*, two-tailed unpaired T-test or U Mann-Whitney test). V, cortical layer V,
839 V*rest*, resting membrane potential; APamp, action potential amplitude. Scale bar:
840 100 µm. ***See also Figure supplement 1 and table supplement 1.***

841

842 ***Figure 2. Reduced basal dendritic complexity of layer V pyramidal neurons***
843 ***(LVPNs) in Nr2f1 mutant cortices.*** *R*epresentative images of *Ctrl* **(A)** and *Nr2f1cKO*
844 **(B)** LVPNs. In grayscale, maximum intensity projection of a multi-stack confocal
845 image; in green, correspondent 3D reconstructions. On the right, magnifications of
846 the basal structures. Scale bar: 50 m. **C)** Sholl analysis points to a reduction of the
847 arborization complexity of *Nr2f1cKO* LVPNs (** P = 0.002; **** P < 0.0001). **D**) Basal
848 Dendrite Complexity Index (DCI) formula and schematic representation of primary
849 dendrites, branching points, terminal tips and tip orders. **E-H**) Average basal DCI (**
850 P = 0.0019), number of primary dendrites (* P = 0.0159)**,** basal dendrites branching
851 point (*** P = 0.0004) and terminal tips (*** P = 0.0009) are statistically reduced in
852 mutant cells compared to controls. (N = 15 *Ctrl*, N = 28 *Nr2f1cKO*). P-values are
853 calculated by 2way ANOVA test **(C)**, Mann-Whitney non parametric test **(E)** or
854 Welch's unequal variances t-test **(F-H).** ***See also Figure supplement 1.***

855

856 ***Figure 3. Abnormal structural features of the axon initial segment (AIS) in***
857 ***mutant Nr2f1 layer V pyramidal neurons.*** **A**) Left panel, coronal sections of P7
858 somatosensory *Ctrl* and corresponding *Nr2f1cKO* cortices labelled with CTIP2, for
859 layer V identification, Ankyrin G for the AIS and NeuN as a somatic marker. Scale

860 bar: 100 m. Right panel confocal images of triple stained *Ctrl* and *Nr2f1cKO* LVPNs.
861 Scale bar: 10 m. **B-C**) Average AIS length (* P=0.0129) and diameter (** P = 0.0043)
862 are statistically reduced in *Nr2fcKO* neurons compared to *Ctrl* at P7. N=3. **D**)
863 Confocal images of *Ctrl* (left) and *Nr2f1cKO* (right) LVPNs from P21 somatosensory
864 cortices. In green Thy1-eYFP reporter gene, in red Ankyrin G. **E-F**) Average AIS
865 length (**** P < 0.0001) and diameter (**** P < 0.0001) are statistically reduced in
866 *Nr2f1cKO* cells compared to controls at P21. N=3. **G**) Confocal images of control and
867 *Nr2f1cKO* LVPNs non-treated (-KCl) and treated (+KCl) with high KCl aCSF. In green
868 CTIP2, in red Ankyrin G. **H**) Average relative length (average length values were
869 normalized on control values) are significantly reduced in controls after KCl
870 treatment (**** P 0.0001). No differences were observed in *Nr2f1cKO* cells
871 between non-treated and treated populations. (ns P=0.289). P-values are quantified
872 by the Welch's unequal variance t-test (**B**), Unpaired t-test (**C-F**) or 2way ANOVA test
873 (**H**).
874
875 ***Figure 4. Nr2f1 regulates the expression of a subset of ion channels.*** **A**) Data plot
876 of qPCR analysis on P7 *Ctrl* and *Nr2f1cKO* P7 cortices. N≥3. The red line represents
877 the threshold. Significantly downregulated genes are depicted in the upper-left
878 panel. **B**) Western-blot analysis of HCN1 protein shows a significant reduction in
879 *Nr2f1cKO* P7 cortices (*P=0.05). N=4. **C**) CTIP2-HCN1 double IF staining of P7
880 somatosensory cortices. **D**) Dot plot distribution of HCN1 cell signal intensity points
881 to a reduction of HCN1 in *Nr2f1cKO* LVPNs (**** P < 0.0001). N=3. **E**) Snapshots from
882 Evolutionary Conserved Regions (ECR) browser showing Nr2f1 binding location and
883 sites (in pink); intergenic regions (red); UTR (yellow); exons (blue); introns
884 (orange). **F**) Graph showing the ratio between unspecific and specific antibody (a.b.)
885 fold changes (f.c.) on Nr2f1 consensus sites. N=3. P-values are calculated by Welch's
886 unequal variances t-test (B-E), unpaired (A) or paired (F) t-test followed by
887 Benjamini–Hochberg multiple test correction, false discovery rate = 0.25. ***See also***
888 ***figure supplement 1***.
889
890 ***Figure 5. Altered Ca^{2+}-dependent intrinsic activity upon Nr2f1 loss.*** **A**) Schematic
891 and representative images of Ca^{2+} BAPTA fluorescent signals in an acute horizontal
892 slice preparation from somatosensory cortex. On the right, time series of

893 intracellular signal in manually defined cells, corrected by moving average (Fi).
894 Bursting events are defined by distinct thresholds. Below, time series matrices of
895 above threshold Ca^{2+} signals with interneuron unsupervised hierarchical clustering
896 (left). Interneuron Pearson correlation matrices (right). P1 and P4 were analyzed
897 independently, *Ctrl* and *Nr2f1cKO* frequency and correlation score quantified by
898 Welch Two-samples test. hierarchical clustering performed with Euclidean distance,
899 using average, burst frequency and correlation per condition. Statistical scripts were
900 custom-prepared in R (Computing, 2018). **B, C**) Distribution of single cell Ca^{2+} burst
901 frequency (**B**) and burst intra-neuron correlation (**C**) in P1 and P4 brains. **D**)
902 Unsupervised hierarchical clustering of Ca^{2+} burst frequency and intra-neuron burst
903 correlation.
904
905 ***Figure 6. Impaired intrinsic network and bursting activity recorded in DIV 9***
906 ***cultured Nr2f1-deficient cortical neurons.*** **A**) Spontaneous firing of *Ctrl* (left) and
907 *Nr2f1cKO* (right) cortical network was recorded by three representative MEA
908 electrodes a 9DIV. In insets, representative bursts are shown at expanded scale. **B-F**)
909 Firing parameters measured in *Ctrl* and *Nr2f1cKO* cortical networks are compared (*
910 P<0.05; **P<0.01, unpaired T-test). ***See also figure supplement 1.***
911 **SUPPLEMENTAL FIGURES:**
912
913 ***Figure 1 – supplement 1. Specific intrinsic excitability features and input-output***
914 ***relationship remain unlatered in Nr2f1 deficient layer V pyramidal neurons***
915 ***(LVPNs).*** **A**) LVPNs in *Ctrl* (in black) and *Nr2f1cKO* (in red) display normal input
916 resistance and threshold for action potential and inter-spike interval. We observed a
917 tendency of *Nr2f1cKO* LVPNs to display a reduced half-width of action potential when
918 compared to *Ctrl* LVPNs (P = 0.066) and a significant decreased AP*amp* (* *P* =
919 0.04441) measured from resting membrane protential (N = 19 *Ctrl*, N = 28 *Nr2f1cKO*,
920 two-tailed unpaired T-test or U Mann-Whitney test). **B**) Input/output function is not
921 significantly different between *Nr2f1cKO* LVPNs and *Ctrl* LVPNs (N = 19 *Ctrl*, N = 28
922 *Nr2f1cKO*, two-way ANOVA). R*in*, input resistance; V*threshold*, threshold for action
923 potential; AP*h-w*, half-width of action potential; ISI, inter-spike interval.
924
925 ***Figure 1 –table supplement 1.*** Intrinsic electrophysiological properties of layer V

926 pyramidal neurons in *ex vivo Ctrl* and *Nr2f1cKO* brain slices.

927

928 ***Figure 2 – figure supplement 1. Apical dendritic complexity of layer V pyramidal***
929 ***neurons (LVPNs) is not affected in Nr2f1 mutant brains.*** **A**) Sholl analysis shows
930 no differences in complexity between *Ctrl* and *Nr2f1cKO* LVPNs, relatively to distal
931 dendrites. (ns P > 0.5) **B-D**) Number of Apical Branching Points (ns P = 0.57), Apical
932 Terminal Tips (ns P = 0.70) and Lateral dendrites (ns P =0.20) are unaffected by the
933 loss of *Nr2f1* (N = 12 *Ctrl*, N = 24 *Nr2f1cKO*). P-values are calculated by 2way ANOVA
934 test (**A**) or Welch's unequal variances t-test (**B-D**).

935

936 ***Figure 4 - figure supplement 1. qPCR quantification of cortical ion channels in***
937 ***Nr2f1 mutant cortices.*** Single qPCR quantification of P7 *Ctrl* vs *Nr2f1cKO*
938 expression of chosen cortically expressed ion channel subunits and Glutamate
939 receptors. *Ctrl* mean value is normalized to 1 to calculate fold changes in *Nr2f1cKO*
940 conditions. N≥3. Statistical significance is tested doing paired t-test with P-value
941 adjusted according to Benjamini–Hochberg procedure. *- P-Value < 0.05. P –
942 Postnatal day.

943

944 ***Figure 6- figure supplement 1. Impaired intrinsic network and bursting activity***
945 ***recorded in DIV15 cultured Nr2f1-deficient cortical neurons.*** **A**) Spontaneous
946 firing of *Ctrl* (left) and *Nr2f1cKO* (right) cortical network was recorded by three
947 representative MEA electrodes a 15DIV. In insets, representative bursts are shown
948 at expanded scale. **B-F**) Firing parameters measured in *Ctrl* and *Nr2f1cKO* cortical
949 networks are compared (* P<0.05; ***P<0.001, unpaired T-test)

950

951 **Key resources table.** List of antibodies used in this study.

952 **REFERENCES:**

953 ALFANO, C., MAGRINELLI, E., HARB, K., HEVNER, R. F. & STUDER, M. 2014. Postmitotic
954 control of sensory area specification during neocortical development. *Nat Commun,*
955 5**,** 5632.
956 ALFANO, C. & STUDER, M. 2012. Neocortical arealization: Evolution, mechanisms and open
957 questions. *Dev Neurobiol*.
958 ALFANO, C., VIOLA, L., HENG, J. I., PIROZZI, M., CLARKSON, M., FLORE, G., DE MAIO, A.,
959 SCHEDL, A., GUILLEMOT, F. & STUDER, M. 2011. COUP-TFI promotes radial
960 migration and proper morphology of callosal projection neurons by repressing Rnd2
961 expression. *Development,* 138**,** 4685-97.
962 ALLENE, C., CATTANI, A., ACKMAN, J. B., BONIFAZI, P., ANIKSZTEJN, L., BEN-ARI, Y. &
963 COSSART, R. 2008. Sequential generation of two distinct synapse-driven network
964 patterns in developing neocortex. *J Neurosci,* 28**,** 12851-63.
965 ALLENE, C. & COSSART, R. 2010. Early NMDA receptor-driven waves of activity in the
966 developing neocortex: physiological or pathological network oscillations? *J Physiol,*
967 588**,** 83-91.
968 ANDERSON, O. D. 1975. Moving Average Processes. The Statistician.
969 ANDREAE, L. C. & BURRONE, J. 2018. The role of spontaneous neurotransmission in synapse
970 and circuit development. *J Neurosci Res,* 96**,** 354-359.
971 ANTON-BOLANOS, N., SEMPERE-FERRANDEZ, A., GUILLAMON-VIVANCOS, T., MARTINI, F. J.,
972 PEREZ-SAIZ, L., GEZELIUS, H., FILIPCHUK, A., VALDEOLMILLOS, M. & LOPEZ-
973 BENDITO, G. 2019. Prenatal activity from thalamic neurons governs the emergence
974 of functional cortical maps in mice. *Science,* 364**,** 987-990.
975 ARLOTTA, P., MOLYNEAUX, B. J., CHEN, J., INOUE, J., KOMINAMI, R. & MACKLIS, J. D. 2005.
976 Neuronal subtype-specific genes that control corticospinal motor neuron
977 development in vivo. *Neuron,* 45**,** 207-21.
978 ARMENTANO, M., CHOU, S. J., TOMASSY, G. S., LEINGARTNER, A., O'LEARY, D. D. & STUDER,
979 M. 2007. COUP-TFI regulates the balance of cortical patterning between
980 frontal/motor and sensory areas. *Nat Neurosci,* 10**,** 1277-86.
981 ARNOLD, E. C., MCMURRAY, C., GRAY, R. & JOHNSTON, D. 2019. Epilepsy-Induced Reduction
982 in HCN Channel Expression Contributes to an Increased Excitability in Dorsal, But
983 Not Ventral, Hippocampal CA1 Neurons. *eNeuro,* 6.
984 BENDER, R. A. & BARAM, T. Z. 2008. Hyperpolarization activated cyclic-nucleotide gated
985 (HCN) channels in developing neuronal networks. *Prog Neurobiol,* 86**,** 129-40.
986 BERGER, T., LARKUM, M. E. & LUSCHER, H. R. 2001. High I(h) channel density in the distal
987 apical dendrite of layer V pyramidal cells increases bidirectional attenuation of
988 EPSPs. *J Neurophysiol,* 85**,** 855-68.
989 BERTACCHI, M., PARISOT, J. & STUDER, M. 2019. The pleiotropic transcriptional regulator
990 COUP-TFI plays multiple roles in neural development and disease. *Brain Res,* 1705**,**
991 75-94.
992 BLANKENSHIP, A. G., HAMBY, A. M., FIRL, A., VYAS, S., MAXEINER, S., WILLECKE, K. &
993 FELLER, M. B. 2011. The role of neuronal connexins 36 and 45 in shaping
994 spontaneous firing patterns in the developing retina. *J Neurosci,* 31**,** 9998-10008.
995 BOILLOT, M., LEE, C. Y., ALLENE, C., LEGUERN, E., BAULAC, S. & ROUACH, N. 2016. LGI1 acts
996 presynaptically to regulate excitatory synaptic transmission during early postnatal
997 development. *Sci Rep,* 6**,** 21769.
998 BOSCH, D. G., BOONSTRA, F. N., DE LEEUW, N., PFUNDT, R., NILLESEN, W. M., DE LIGT, J.,
999 GILISSEN, C., JHANGIANI, S., LUPSKI, J. R., CREMERS, F. P. & DE VRIES, B. B. 2016.
1000 Novel genetic causes for cerebral visual impairment. *Eur J Hum Genet,* 24**,** 660-5.
1001 BOSCH, D. G., BOONSTRA, F. N., GONZAGA-JAUREGUI, C., XU, M., DE LIGT, J., JHANGIANI, S.,
1002 WISZNIEWSKI, W., MUZNY, D. M., YNTEMA, H. G., PFUNDT, R., VISSERS, L. E.,
1003 SPRUIJT, L., BLOKLAND, E. A., CHEN, C. A., BAYLOR-HOPKINS CENTER FOR
1004 MENDELIAN, G., LEWIS, R. A., TSAI, S. Y., GIBBS, R. A., TSAI, M. J., LUPSKI, J. R.,

ZOGHBI, H. Y., CREMERS, F. P., DE VRIES, B. B. & SCHAAF, C. P. 2014. NR2F1 mutations cause optic atrophy with intellectual disability. *Am J Hum Genet,* 94**,** 303-9.

BOYCHUK, J. A., FARRELL, J. S., PALMER, L. A., SINGLETON, A. C., PITTMAN, Q. J. & TESKEY, G. C. 2017. HCN channels segregate stimulation-evoked movement responses in neocortex and allow for coordinated forelimb movements in rodents. *J Physiol,* 595**,** 247-263.

BRAGER, D. H., AKHAVAN, A. R. & JOHNSTON, D. 2012. Impaired dendritic expression and plasticity of h-channels in the fmr1(-/y) mouse model of fragile X syndrome. *Cell Rep,* 1**,** 225-33.

BRAGER, D. H. & JOHNSTON, D. 2007. Plasticity of intrinsic excitability during long-term depression is mediated through mGluR-dependent changes in I(h) in hippocampal CA1 pyramidal neurons. *J Neurosci,* 27**,** 13926-37.

CHEN, C. A., BOSCH, D. G., CHO, M. T., ROSENFELD, J. A., SHINAWI, M., LEWIS, R. A., MANN, J., JAYAKAR, P., PAYNE, K., WALSH, L., MOSS, T., SCHREIBER, A., SCHOONVELD, C., MONAGHAN, K. G., ELMSLIE, F., DOUGLAS, G., BOONSTRA, F. N., MILLAN, F., CREMERS, F. P., MCKNIGHT, D., RICHARD, G., JUUSOLA, J., KENDALL, F., RAMSEY, K., ANYANE-YEBOA, K., MALKIN, E., CHUNG, W. K., NIYAZOV, D., PASCUAL, J. M., WALKIEWICZ, M., VELUCHAMY, V., LI, C., HISAMA, F. M., DE VRIES, B. B. & SCHAAF, C. 2016. The expanding clinical phenotype of Bosch-Boonstra-Schaaf optic atrophy syndrome: 20 new cases and possible genotype-phenotype correlations. *Genet Med*.

CHEN, K., ARADI, I., THON, N., EGHBAL-AHMADI, M., BARAM, T. Z. & SOLTESZ, I. 2001. Persistently modified h-channels after complex febrile seizures convert the seizure-induced enhancement of inhibition to hyperexcitability. *Nat Med,* 7**,** 331-7.

CHO, M. W. & CHOI, M. Y. 2012. Spontaneous organization of the cortical structure through endogenous neural firing and gap junction transmission. *Neural Netw,* 31**,** 46-52.

COMPUTING, R. F. F. S. 2018. R: A Language and Environment for Statistical Computing. R Foundation for Statistical Computing.

CONTESSE, T., AYRAULT, M., MANTEGAZZA, M., STUDER, M. & DESCHAUX, O. 2019. Hyperactive and anxiolytic-like behaviors result from loss of COUP-TFI/Nr2f1 in the mouse cortex. *Genes Brain Behav***,** e12556.

CORLEW, R., BOSMA, M. M. & MOODY, W. J. 2004. Spontaneous, synchronous electrical activity in neonatal mouse cortical neurones. *J Physiol,* 560**,** 377-90.

DEL PINO, I., BROTONS-MAS, J. R., MARQUES-SMITH, A., MARIGHETTO, A., FRICK, A., MARIN, O. & RICO, B. 2017. Abnormal wiring of CCK(+) basket cells disrupts spatial information coding. *Nat Neurosci,* 20**,** 784-792.

DEL PINO, I., GARCIA-FRIGOLA, C., DEHORTER, N., BROTONS-MAS, J. R., ALVAREZ-SALVADO, E., MARTINEZ DE LAGRAN, M., CICERI, G., GABALDON, M. V., MORATAL, D., DIERSSEN, M., CANALS, S., MARIN, O. & RICO, B. 2013. Erbb4 deletion from fast-spiking interneurons causes schizophrenia-like phenotypes. *Neuron,* 79**,** 1152-68.

DUMITRESCU, A. S., EVANS, M. D. & GRUBB, M. S. 2016. Evaluating Tools for Live Imaging of Structural Plasticity at the Axon Initial Segment. *Front Cell Neurosci,* 10**,** 268.

FAEDO, A., TOMASSY, G. S., RUAN, Y., TEICHMANN, H., KRAUSS, S., PLEASURE, S. J., TSAI, S. Y., TSAI, M. J., STUDER, M. & RUBENSTEIN, J. L. 2008. COUP-TFI coordinates cortical patterning, neurogenesis, and laminar fate and modulates MAPK/ERK, AKT, and beta-catenin signaling. *Cereb Cortex,* 18**,** 2117-31.

FAN, J., STEMKOWSKI, P. L., GANDINI, M. A., BLACK, S. A., ZHANG, Z., SOUZA, I. A., CHEN, L. & ZAMPONI, G. W. 2016. Reduced Hyperpolarization-Activated Current Contributes to Enhanced Intrinsic Excitability in Cultured Hippocampal Neurons from PrP(-/-) Mice. *Front Cell Neurosci,* 10**,** 74.

FAN, Y., FRICKER, D., BRAGER, D. H., CHEN, X., LU, H. C., CHITWOOD, R. A. & JOHNSTON, D. 2005. Activity-dependent decrease of excitability in rat hippocampal neurons through increases in I(h). *Nat Neurosci,* 8**,** 1542-51.

FAZEL DARBANDI, S., ROBINSON SCHWARTZ, S. E., QI, Q., CATTA-PRETA, R., PAI, E. L., MANDELL, J. D., EVERITT, A., RUBIN, A., KRASNOFF, R. A., KATZMAN, S., TASTAD, D.,

NORD, A. S., WILLSEY, A. J., CHEN, B., STATE, M. W., SOHAL, V. S. & RUBENSTEIN, J. L. R. 2018. Neonatal Tbr1 Dosage Controls Cortical Layer 6 Connectivity. *Neuron,* 100**,** 831-845.e7.

FLORE, G., DI RUBERTO, G., PARISOT, J., SANNINO, S., RUSSO, F., ILLINGWORTH, E. A., STUDER, M. & DE LEONIBUS, E. 2017. Gradient COUP-TFI Expression Is Required for Functional Organization of the Hippocampal Septo-Temporal Longitudinal Axis. *Cereb Cortex,* 27**,** 1629-1643.

GAVELLO, D., CALORIO, C., FRANCHINO, C., CESANO, F., CARABELLI, V., CARBONE, E. & MARCANTONI, A. 2018. Early Alterations of Hippocampal Neuronal Firing Induced by Abeta42. *Cereb Cortex,* 28**,** 433-446.

GAVELLO, D., ROJO-RUIZ, J., MARCANTONI, A., FRANCHINO, C., CARBONE, E. & CARABELLI, V. 2012. Leptin counteracts the hypoxia-induced inhibition of spontaneously firing hippocampal neurons: a microelectrode array study. *PLoS One,* 7**,** e41530.

GREIG, L. C., WOODWORTH, M. B., GALAZO, M. J., PADMANABHAN, H. & MACKLIS, J. D. 2013. Molecular logic of neocortical projection neuron specification, development and diversity. *Nat Rev Neurosci,* 14**,** 755-69.

GROC, L., PETANJEK, Z., GUSTAFSSON, B., BEN-ARI, Y., HANSE, E. & KHAZIPOV, R. 2002. In vivo blockade of neural activity alters dendritic development of neonatal CA1 pyramidal cells. *Eur J Neurosci,* 16**,** 1931-8.

GRUBB, M. S. & BURRONE, J. 2010. Activity-dependent relocation of the axon initial segment fine-tunes neuronal excitability. *Nature,* 465**,** 1070-4.

GULLEDGE, A. T. & BRAVO, J. J. 2016. Neuron Morphology Influences Axon Initial Segment Plasticity. *eNeuro,* 3.

HAMADA, M. S., GOETHALS, S., DE VRIES, S. I., BRETTE, R. & KOLE, M. H. 2016. Covariation of axon initial segment location and dendritic tree normalizes the somatic action potential. *Proc Natl Acad Sci U S A,* 113**,** 14841-14846.

HARB, K., MAGRINELLI, E., NICOLAS, C. S., LUKIANETS, N., FRANGEUL, L., PIETRI, M., SUN, T., SANDOZ, G., GRAMMONT, F., JABAUDON, D., STUDER, M. & ALFANO, C. 2016. Area-specific development of distinct projection neuron subclasses is regulated by postnatal epigenetic modifications. *Elife,* 5**,** e09531.

JABAUDON, D. 2017. Fate and freedom in developing neocortical circuits. *Nat Commun,* 8**,** 16042.

KIRISCHUK, S., SINNING, A., BLANQUIE, O., YANG, J. W., LUHMANN, H. J. & KILB, W. 2017. Modulation of Neocortical Development by Early Neuronal Activity: Physiology and Pathophysiology. *Front Cell Neurosci,* 11**,** 379.

KIRKBY, L. A., SACK, G. S., FIRL, A. & FELLER, M. B. 2013. A role for correlated spontaneous activity in the assembly of neural circuits. *Neuron,* 80**,** 1129-44.

KLUEVA, J., LIMA, A. D., MEIS, S., VOIGT, T. & MUNSCH, T. 2012. Hyperpolarization-activated cation current contributes to spontaneous network activity in developing neocortical cultures. *Neurosignals,* 20**,** 35-47.

KOLE, M. H. & STUART, G. J. 2012. Signal processing in the axon initial segment. *Neuron,* 73**,** 235-47.

KORDELI, E., LAMBERT, S. & BENNETT, V. 1995. AnkyrinG. A new ankyrin gene with neural-specific isoforms localized at the axonal initial segment and node of Ranvier. *J Biol Chem,* 270**,** 2352-9.

KUBA, H. 2010. Plasticity at the axon initial segment. *Commun Integr Biol,* 3**,** 597-8.

KUBA, H., OICHI, Y. & OHMORI, H. 2010. Presynaptic activity regulates Na(+) channel distribution at the axon initial segment. *Nature,* 465**,** 1075-8.

LI, H., FERTUZINHOS, S., MOHNS, E., HNASKO, T. S., VERHAGE, M., EDWARDS, R., SESTAN, N. & CRAIR, M. C. 2013. Laminar and columnar development of barrel cortex relies on thalamocortical neurotransmission. *Neuron,* 79**,** 970-86.

LOOTS, G. & OVCHARENKO, I. 2007. ECRbase: database of evolutionary conserved regions, promoters, and transcription factor binding sites in vertebrate genomes. *Bioinformatics,* 23**,** 122-4.

LUHMANN, H. J. & KHAZIPOV, R. 2018. Neuronal activity patterns in the developing barrel cortex. *Neuroscience,* 368**,** 256-267.
LUHMANN, H. J., SINNING, A., YANG, J. W., REYES-PUERTA, V., STUTTGEN, M. C., KIRISCHUK, S. & KILB, W. 2016. Spontaneous Neuronal Activity in Developing Neocortical Networks: From Single Cells to Large-Scale Interactions. *Front Neural Circuits,* 10**,** 40.
MAGEE, J. C. 1998. Dendritic hyperpolarization-activated currents modify the integrative properties of hippocampal CA1 pyramidal neurons. *J Neurosci,* 18**,** 7613-24.
MOODY, W. J. & BOSMA, M. M. 2005. Ion channel development, spontaneous activity, and activity-dependent development in nerve and muscle cells. *Physiol Rev,* 85**,** 883-941.
MURASE, S., LANTZ, C. L., KIM, E., GUPTA, N., HIGGINS, R., STOPFER, M., HOFFMAN, D. A. & QUINLAN, E. M. 2016. Matrix Metalloproteinase-9 Regulates Neuronal Circuit Development and Excitability. *Mol Neurobiol,* 53**,** 3477-3493.
O'LEARY, D. D. & SAHARA, S. 2008. Genetic regulation of arealization of the neocortex. *Curr Opin Neurobiol,* 18**,** 90-100.
OVCHARENKO, I., NOBREGA, M. A., LOOTS, G. G. & STUBBS, L. 2004. ECR Browser: a tool for visualizing and accessing data from comparisons of multiple vertebrate genomes. *Nucleic Acids Res,* 32**,** W280-6.
PEARSON, R. A., CATSICAS, M., BECKER, D. L., BAYLEY, P., LUNEBORG, N. L. & MOBBS, P. 2004. Ca(2+) signalling and gap junction coupling within and between pigment epithelium and neural retina in the developing chick. *Eur J Neurosci,* 19**,** 2435-45.
POOLOS, N. P., BULLIS, J. B. & ROTH, M. K. 2006. Modulation of h-channels in hippocampal pyramidal neurons by p38 mitogen-activated protein kinase. *J Neurosci,* 26**,** 7995-8003.
POOLOS, N. P., MIGLIORE, M. & JOHNSTON, D. 2002. Pharmacological upregulation of h-channels reduces the excitability of pyramidal neuron dendrites. *Nat Neurosci,* 5**,** 767-74.
ROERIG, B. & FELLER, M. B. 2000. Neurotransmitters and gap junctions in developing neural circuits. *Brain Res Brain Res Rev,* 32**,** 86-114.
SCHINDELIN, J., ARGANDA-CARRERAS, I., FRISE, E., KAYNIG, V., LONGAIR, M., PIETZSCH, T., PREIBISCH, S., RUEDEN, C., SAALFELD, S., SCHMID, B., TINEVEZ, J. Y., WHITE, D. J., HARTENSTEIN, V., ELICEIRI, K., TOMANCAK, P. & CARDONA, A. 2012. Fiji: an open-source platform for biological-image analysis. *Nat Methods,* 9**,** 676-82.
SCHNEGGENBURGER, R. & ROSENMUND, C. 2015. Molecular mechanisms governing Ca(2+) regulation of evoked and spontaneous release. *Nat Neurosci,* 18**,** 935-41.
SHAH, M. M. 2014. Cortical HCN channels: function, trafficking and plasticity. *J Physiol,* 592**,** 2711-9.
SIMI, A. & STUDER, M. 2018. Developmental genetic programs and activity-dependent mechanisms instruct neocortical area mapping. *Curr Opin Neurobiol,* 53**,** 96-102.
TOMASSY, G. S., DE LEONIBUS, E., JABAUDON, D., LODATO, S., ALFANO, C., MELE, A., MACKLIS, J. D. & STUDER, M. 2010. Area-specific temporal control of corticospinal motor neuron differentiation by COUP-TFI. *Proc Natl Acad Sci U S A,* 107**,** 3576-81.
TRITSCH, N. X., YI, E., GALE, J. E., GLOWATZKI, E. & BERGLES, D. E. 2007. The origin of spontaneous activity in the developing auditory system. *Nature,* 450**,** 50-5.
UHLEN, P., FRITZ, N., SMEDLER, E., MALMERSJO, S. & KANATANI, S. 2015. Calcium signaling in neocortical development. *Dev Neurobiol,* 75**,** 360-8.
VALIULLINA, F., AKHMETSHINA, D., NASRETDINOV, A., MUKHTAROV, M., VALEEVA, G., KHAZIPOV, R. & ROZOV, A. 2016. Developmental Changes in Electrophysiological Properties and a Transition from Electrical to Chemical Coupling between Excitatory Layer 4 Neurons in the Rat Barrel Cortex. *Front Neural Circuits,* 10**,** 1.
VAN WELIE, I., REMME, M. W., VAN HOOFT, J. A. & WADMAN, W. J. 2006. Different levels of Ih determine distinct temporal integration in bursting and regular-spiking neurons in rat subiculum. *J Physiol,* 576**,** 203-14.

1165 WANG, Z., XU, N. L., WU, C. P., DUAN, S. & POO, M. M. 2003. Bidirectional changes in spatial
1166 dendritic integration accompanying long-term synaptic modifications. *Neuron,* 37**,**
1167 463-72.
1168 WEFELMEYER, W., PUHL, C. J. & BURRONE, J. 2016. Homeostatic Plasticity of Subcellular
1169 Neuronal Structures: From Inputs to Outputs. *Trends Neurosci,* 39**,** 656-667.
1170 WILLIAMS, S. R. & STUART, G. J. 2000. Site independence of EPSP time course is mediated by
1171 dendritic I(h) in neocortical pyramidal neurons. *J Neurophysiol,* 83**,** 3177-82.
1172 WILLIAMS, S. R. & STUART, G. J. 2003. Voltage- and site-dependent control of the somatic
1173 impact of dendritic IPSPs. *J Neurosci,* 23**,** 7358-67.
1174 YAMADA, R. & KUBA, H. 2016. Structural and Functional Plasticity at the Axon Initial
1175 Segment. *Front Cell Neurosci,* 10**,** 250.
1176 YAMAMOTO, N. & LOPEZ-BENDITO, G. 2012. Shaping brain connections through
1177 spontaneous neural activity. *Eur J Neurosci,* 35**,** 1595-604.
1178 ZHOU, D., LAMBERT, S., MALEN, P. L., CARPENTER, S., BOLAND, L. M. & BENNETT, V. 1998.
1179 AnkyrinG is required for clustering of voltage-gated Na channels at axon initial
1180 segments and for normal action potential firing. *J Cell Biol,* 143**,** 1295-304.

1181

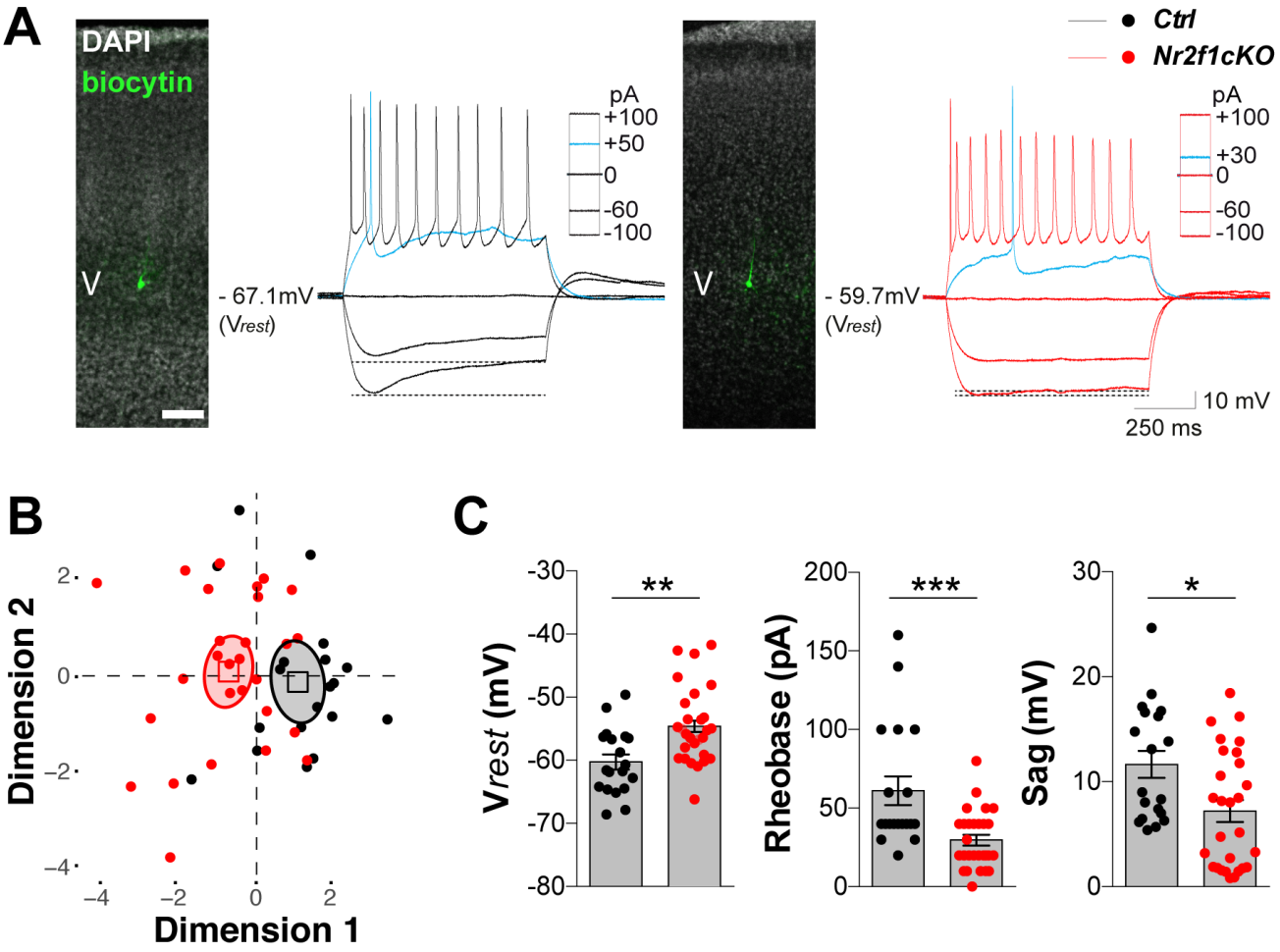
A
DAPI
biocytin
V
- 67.1mV
(Vrest)
pA
+100
+50
0
-60
-100
Ctrl
Nr2f1cKO
V
- 59.7mV
(Vrest)
pA
+100
+30
0
-60
-100
10 mV
250 ms
B
Dimension 2
Dimension 1
C
Vrest (mV)
Rheobase (pA)
Sag (mV)
**
***
*

Figure 1

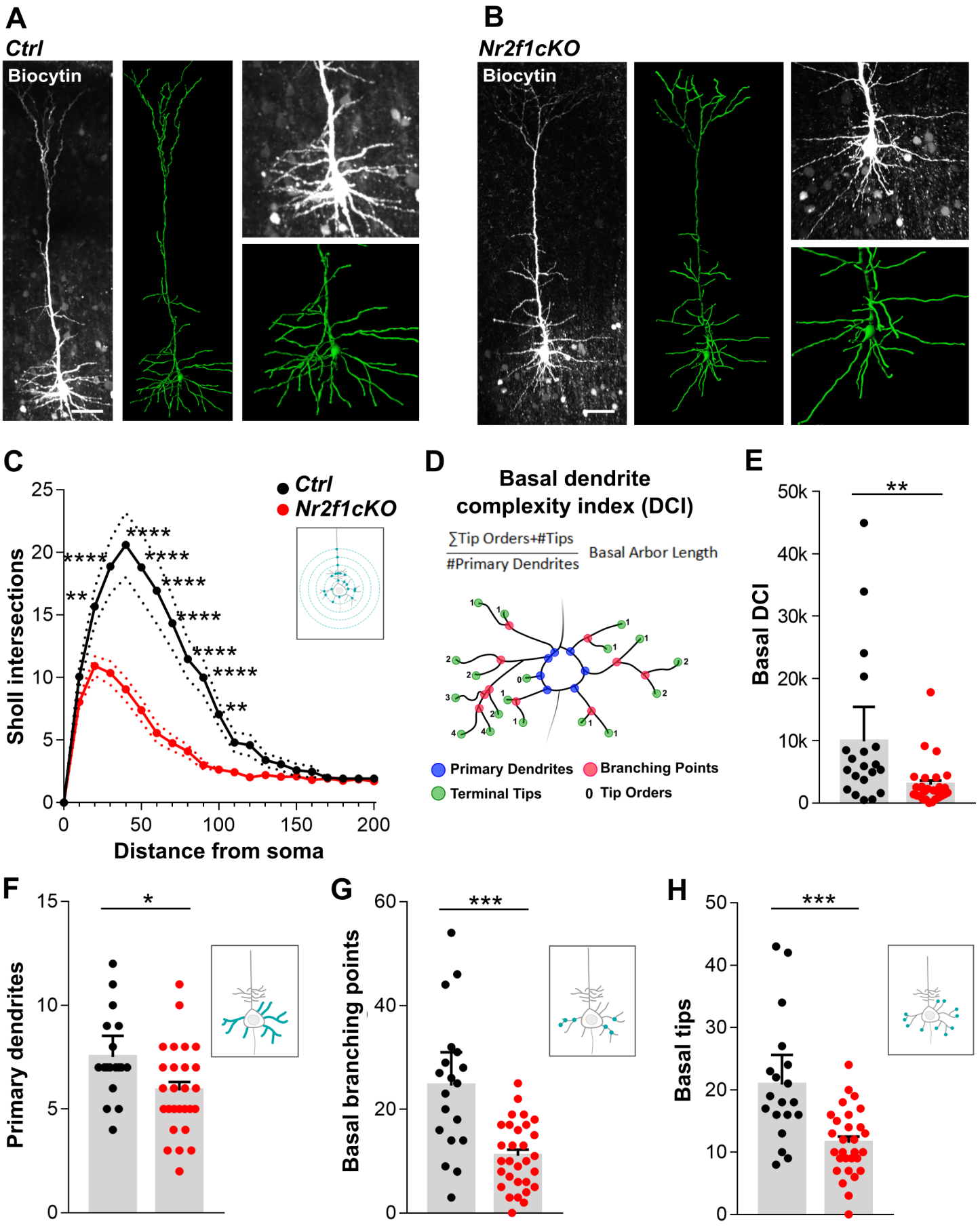
A
Ctrl
Biocytin
B
Nr2f1cKO
Biocytin
C
Ctrl
Nr2f1cKO
Sholl intersections
Distance from soma
D
Basal dendrite complexity index (DCI)
∑Tip Orders+#Tips
#Primary Dendrites
Basal Arbor Length
Primary Dendrites
Branching Points
Terminal Tips
0 Tip Orders
E
Basal DCI
F
Primary dendrites
G
Basal branching points
H
Basal tips

Figure 2

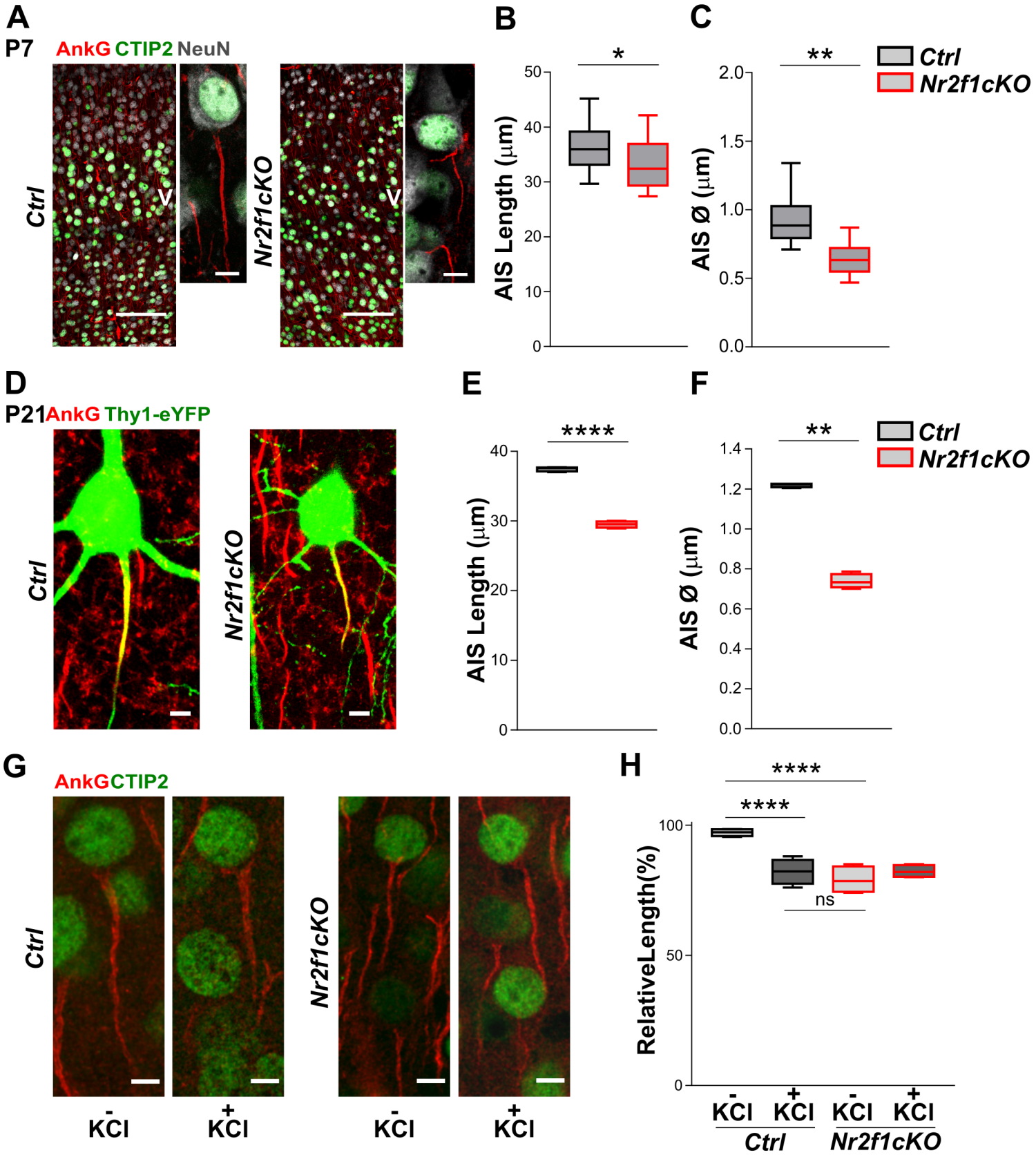
A
P7
AnkG CTIP2 NeuN
Ctrl
V
Nr2f1cKO
V
B
*
AIS Length (μm)
50
40
30
20
10
0
C
**
Ctrl
Nr2f1cKO
AIS Ø (μm)
2.0
1.5
1.0
0.5
0.0
D
P21AnkG Thy1-eYFP
Ctrl
Nr2f1cKO
E
****
AIS Length (μm)
40
30
20
10
0
F
**
Ctrl
Nr2f1cKO
AIS Ø (μm)
1.4
1.2
1.0
0.8
0.6
0.4
0.2
0.0
G
AnkGCTIP2
Ctrl
Nr2f1cKO
-KCl
+KCl
-KCl
+KCl
H
****
****
ns
RelativeLength(%)
100
50
0
-KCl
+KCl
-KCl
+KCl
Ctrl
Nr2f1cKO

Figure 3

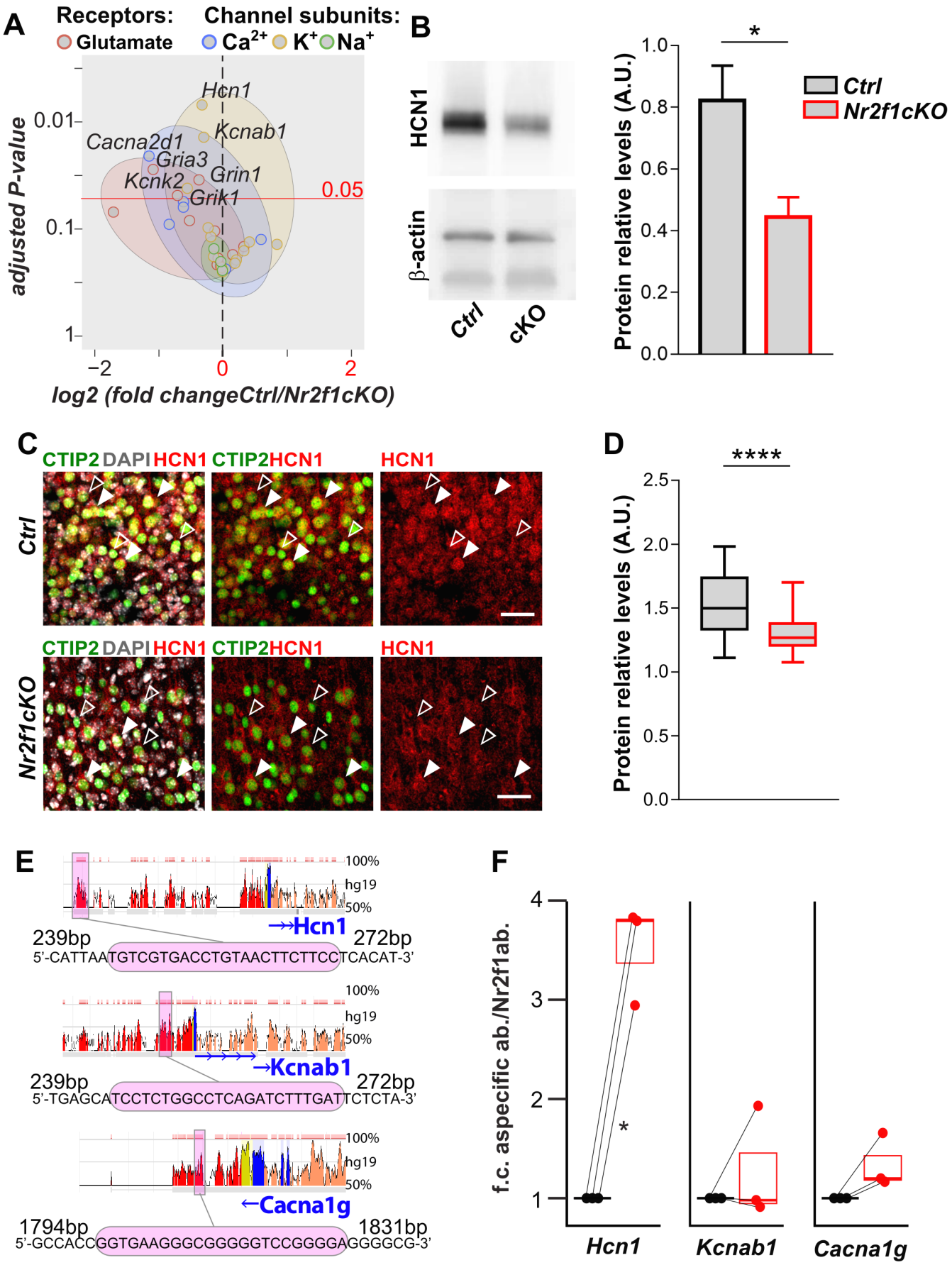
A
Receptors:
Glutamate
Channel subunits:
Ca2+ K+ Na+
Hcn1
Kcnab1
Cacna2d1
Gria3
Kcnk2
Grin1
Grik1
0.05
adjusted P-value
0.01
0.1
1
−2
0
2
log2 (fold changeCtrl/Nr2f1cKO)
B
HCN1
β-actin
Ctrl
cKO
Protein relative levels (A.U.)
1.0
0.8
0.6
0.4
0.2
0.0
*
Ctrl
Nr2f1cKO
C
CTIP2 DAPI HCN1
CTIP2 HCN1
HCN1
Ctrl
Nr2f1cKO
D
****
Protein relative levels (A.U.)
2.5
2.0
1.5
1.0
0.5
0.0
E
100%
hg19
50%
→Hcn1
239bp
272bp
5'-CATTAATGTCGTGACCTGTAACTTCTTCCTCACAT-3'
→Kcnab1
239bp
272bp
5'-TGAGCATCCTCTGGCCTCAGATCTTTGATTCTCTA-3'
←Cacna1g
1794bp
1831bp
5'-GCCACCGGTGAAGGGCGGGGGTCCGGGGAGGGGCG-3'
F
f.c. aspecific ab./Nr2f1ab.
4
3
2
1
*
Hcn1
Kcnab1
Cacna1g

Figure 4

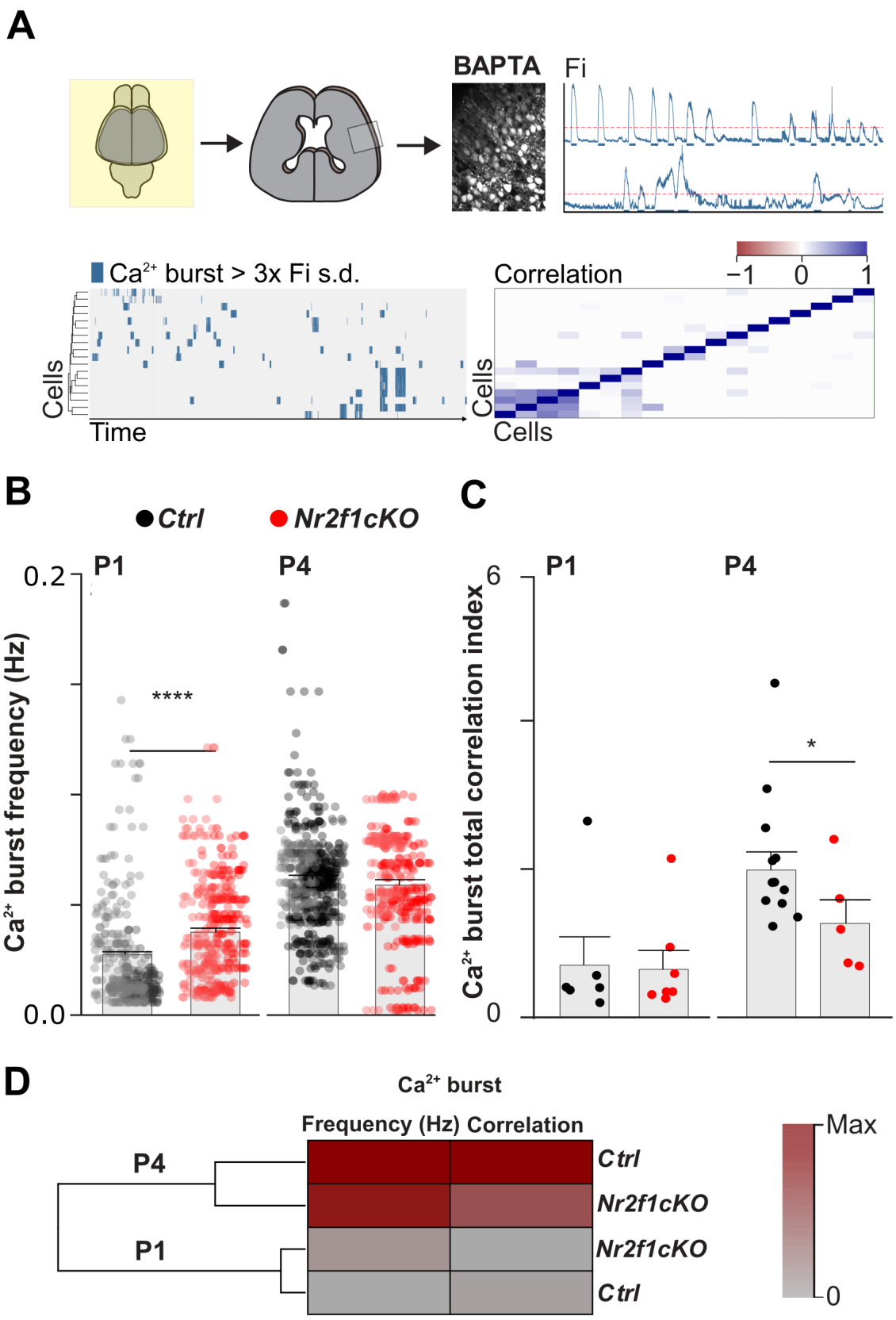
A
BAPTA
Fi
Ca2+ burst > 3x Fi s.d.
Cells
Time
Correlation
−1
0
1
Cells
Cells
B
Ctrl
Nr2f1cKO
P1
P4
0.2
0.0
Ca2+ burst frequency (Hz)
****
C
P1
P4
6
0
Ca2+ burst total correlation index
*
D
Ca2+ burst
Frequency (Hz) Correlation
P4
P1
Ctrl
Nr2f1cKO
Nr2f1cKO
Ctrl
Max
0

Figure 5

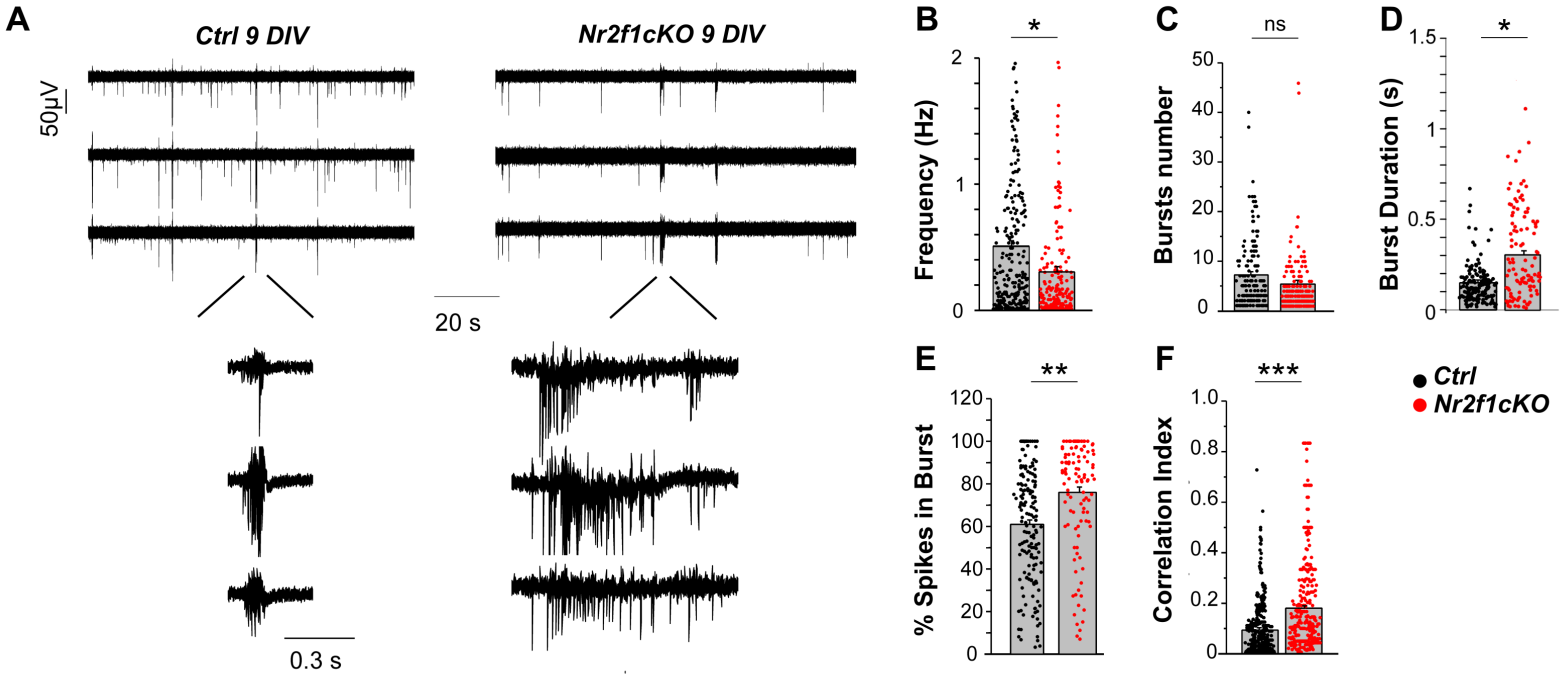
A
Ctrl 9 DIV
Nr2f1cKO 9 DIV
50µV
20 s
0.3 s
B
Frequency (Hz)
*
C
Bursts number
ns
D
Burst Duration (s)
*
E
% Spikes in Burst
**
F
Correlation Index
***
Ctrl
Nr2f1cKO

Figure 6

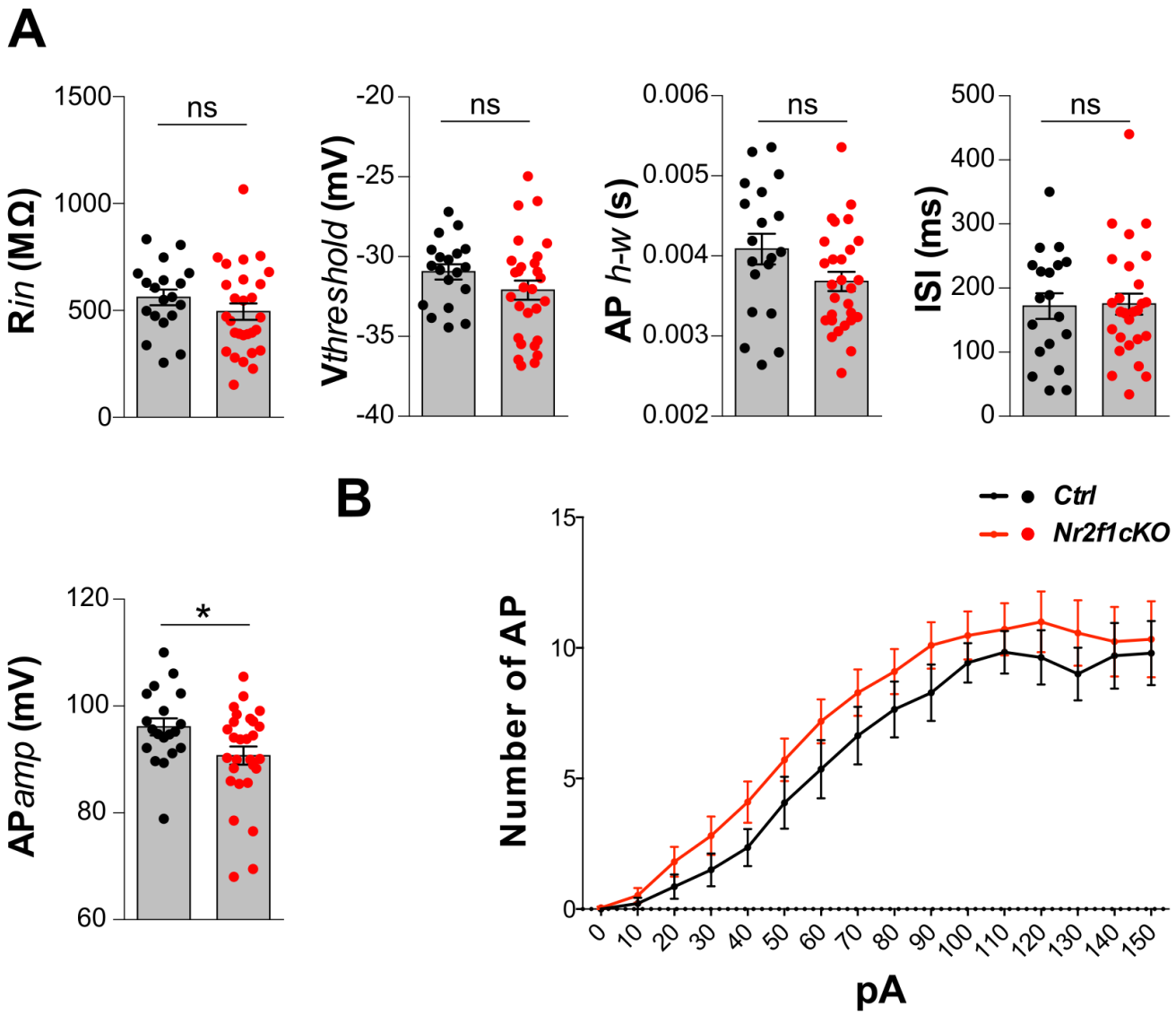

Figure 1 – Supplement 1

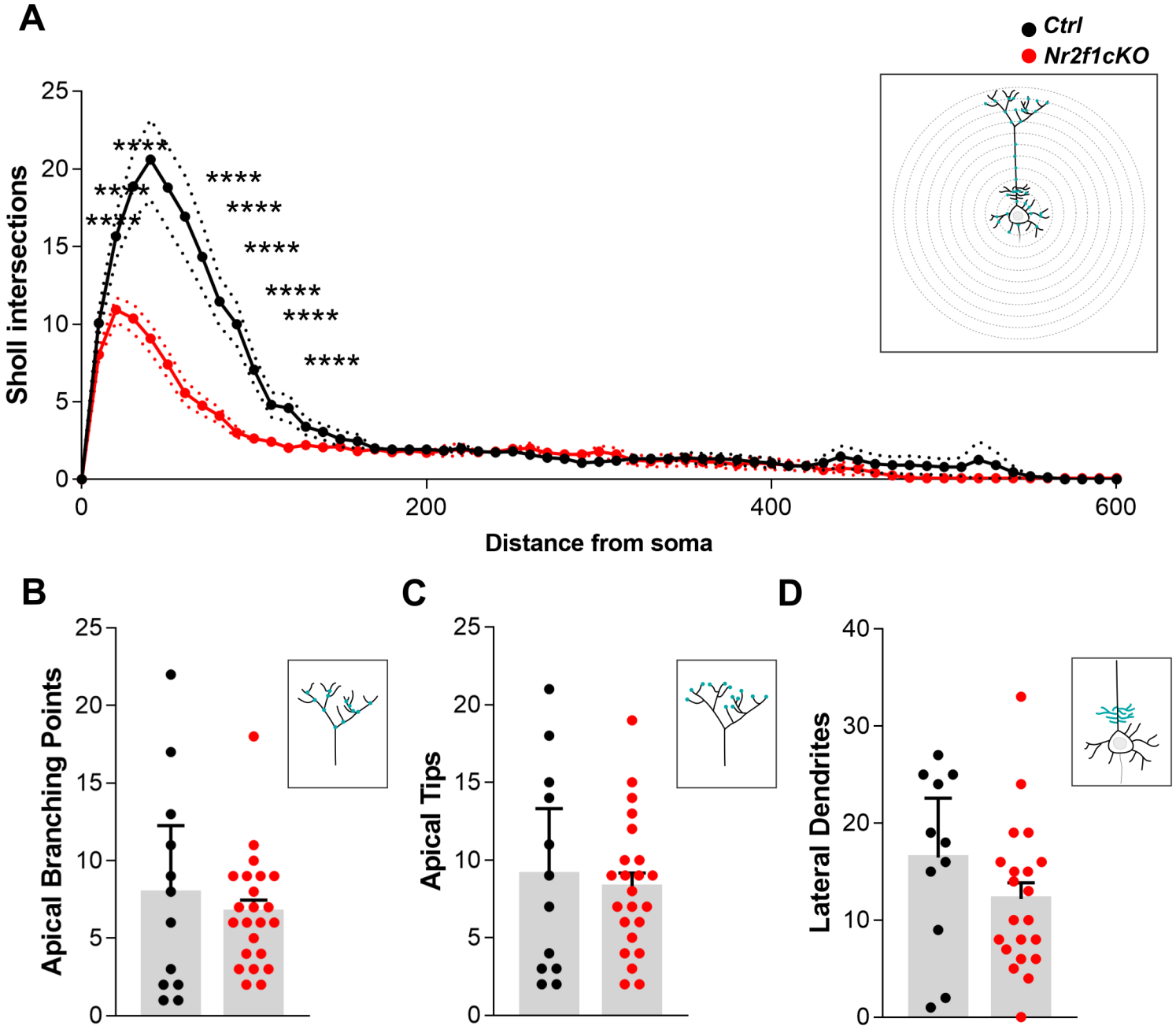

Figure 2 - Supplement 1

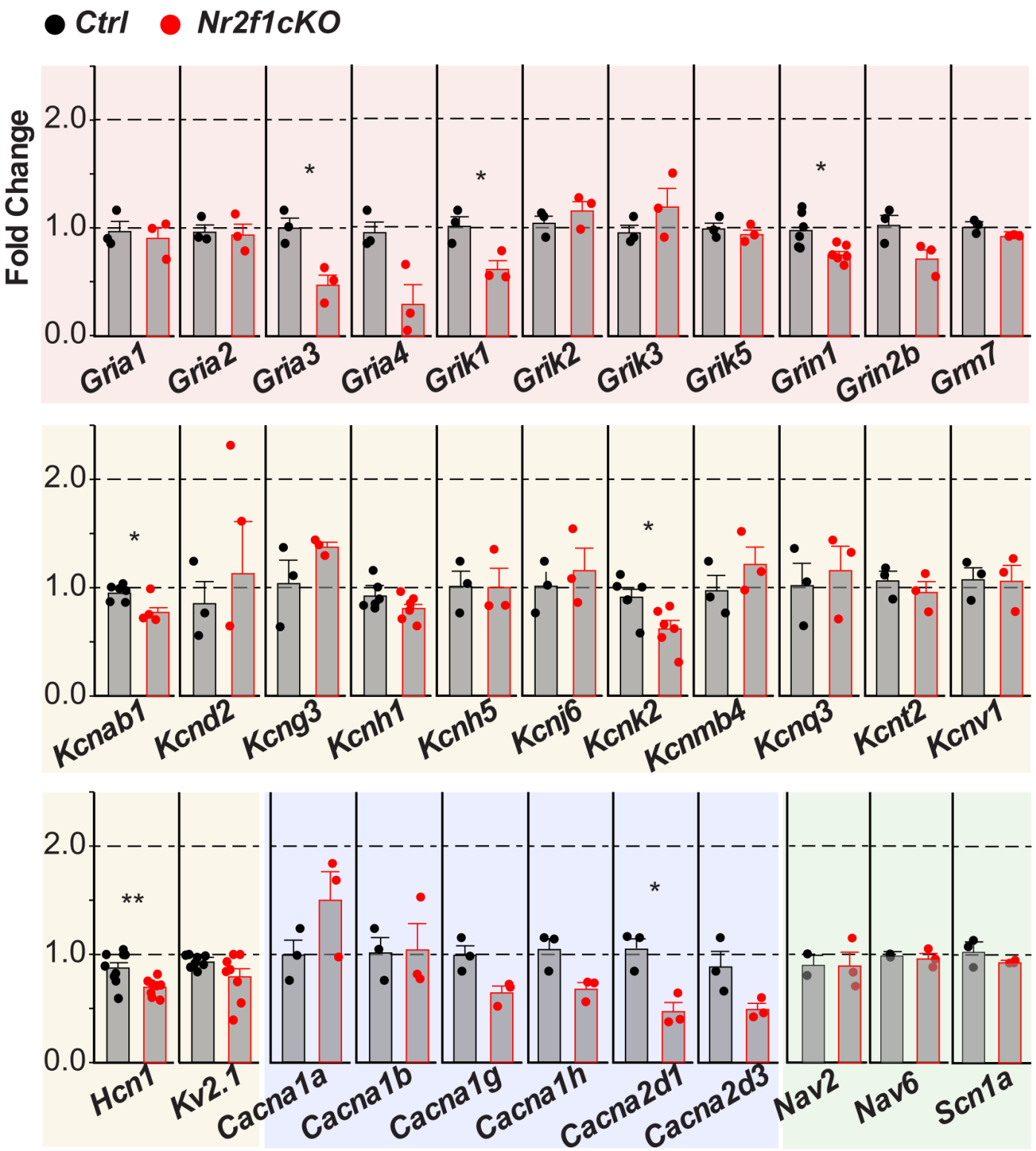

Figure 4 - Supplement 1

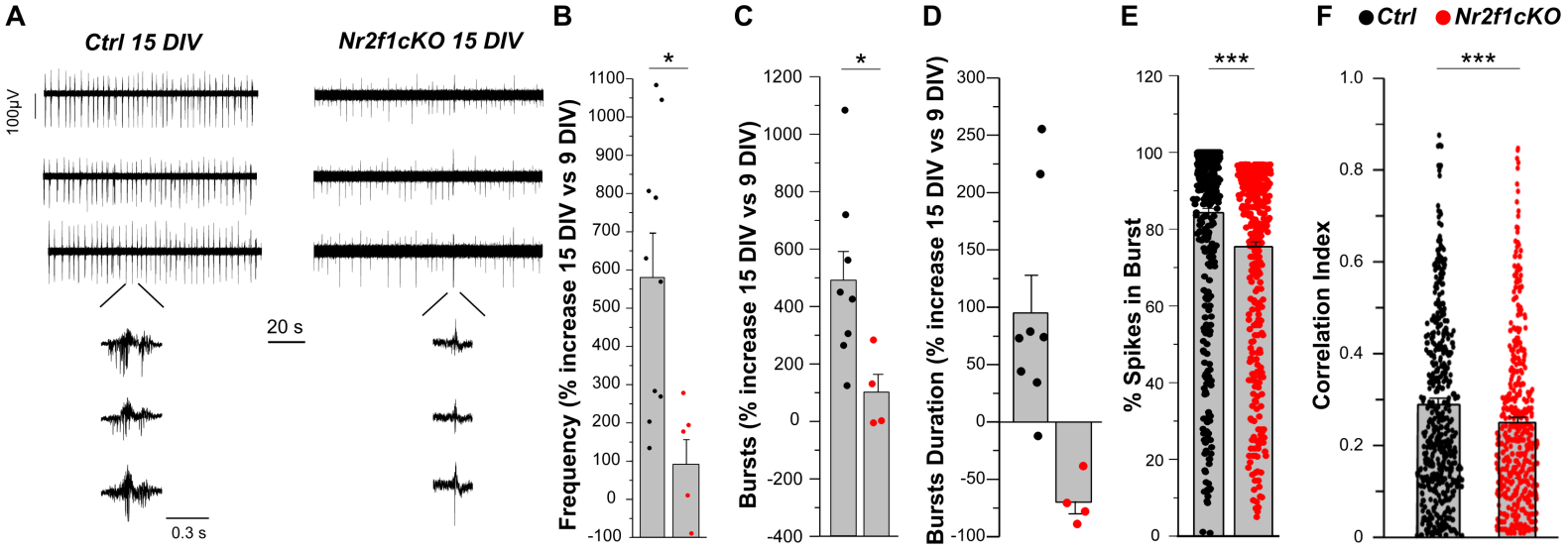

Figure 6 - Supplement 1

	Ctrl	***cKO***	p-value	test
V*rest* (mV)	-60.26 ± 1.18	-54.62 ± 1.13	0.0013 (*)	t-test
R*in* (MΩ)	561.2 ± 36.66	494.80 ± 38.64	0.2410	t-test
Latency (ms)	133.5 ± 15.46	145.9 ± 23.59	0.9023	Mann-Whitney
Rheobase (pA)	61.05 ± 9.08	29.64 ± 3.47	0.001(***)	t-test
V*threshold* (mV)	-30.95 ± 0.48	-32.09 ± 0.60	0.1750	t-test
AP*amp(from* V*threshold)* (mV)	66.65 ± 1.62	69.1 ± 1.11	0.2042	t-test
AP*amp(from* V*rest)* (mV)	96.08 ± 1.611	90.72 ± 1.70	0.0441(*)	Mann-Whitney
Aphalf-width (ms)	0.0041±0.0002	0.0037±0.0001	0.0659	t-test
Inter-spike-interval(ISI) (ms)	172.0 ± 19.92	175.1 ± 16.42	0.9529	Mann-Whitney
Sag (mV)	11.64 ± 1.28	7.2 ± 1.051	0.0103(*)	t-test
τm (ms)	28.42 ± 3.26	31.14 ± 3.70	0.6193	Mann-Whitney